



HAL
open science

Quantifying Thermal Infra-Red directional anisotropy using Master and Landsat-8 simultaneous acquisitions

Julien Michel, Olivier Hagolle, Simon J Hook, Jean-Louis Roujean, Philippe Gamet

► **To cite this version:**

Julien Michel, Olivier Hagolle, Simon J Hook, Jean-Louis Roujean, Philippe Gamet. Quantifying Thermal Infra-Red directional anisotropy using Master and Landsat-8 simultaneous acquisitions. 2023. hal-04073733v2

HAL Id: hal-04073733

<https://hal.science/hal-04073733v2>

Preprint submitted on 22 Jun 2023 (v2), last revised 2 Aug 2023 (v3)

HAL is a multi-disciplinary open access archive for the deposit and dissemination of scientific research documents, whether they are published or not. The documents may come from teaching and research institutions in France or abroad, or from public or private research centers.

L'archive ouverte pluridisciplinaire **HAL**, est destinée au dépôt et à la diffusion de documents scientifiques de niveau recherche, publiés ou non, émanant des établissements d'enseignement et de recherche français ou étrangers, des laboratoires publics ou privés.



Distributed under a Creative Commons Attribution - ShareAlike 4.0 International License

Quantifying Thermal Infra-Red directional anisotropy using Master and Landsat-8 simultaneous acquisitions

Julien Michel^{a,*}, Olivier Hagolle^a, Simon J. Hook^b, Jean-Louis Roujean^a, Philippe Gamet^a

^a*CESBIO, Université de Toulouse, CNES, CNRS, INRAE, IRD, UT3, 18 avenue Edouard Belin, BPI 2801, TOULOUSE Cedex 9, 31401, France*

^b*Jet Propulsion Laboratory, California Institute of Technology, 4800 Oak Grove Drive, Pasadena, CA 91109, United States*

Abstract

Satellite observations in the Thermal Infra-Red (TIR) domain provide valuable information on Land Surface Temperatures, Evapo-Transpiration and water use efficiency and are useful for monitoring vegetation health, agricultural practices and urban planning. By 2030, there will be 3 new high-resolution global coverage satellite TIR missions in space, all of them with fields of view larger than $\pm 30^\circ$. Directional anisotropy in TIR can affect the estimation of key application variables, such as temperature, and are typically studied by means of field campaigns or physical modelling. In this work, we have evaluated directional effects using simultaneous measurements from Landsat-8 and the $\pm 45^\circ$ field of view MASTER airborne TIR sensor from NASA. Differences as high as 6K are observed in the surface temperatures derived from these simultaneous observations. Those differences are attributed to directional effects, with the greatest differences associated with hotspot conditions, where the solar and satellite viewing directions align. Five well studied parametric directional models have then been fitted to the temperature differences, allowing the amplitude of the measured directional effects to be reduced below 1K, with small variations between models. These results suggest that a simple correction for directional effects could be implemented as part of the ground segment processing for the upcoming missions.

Keywords: Thermal Infra-Red, Land Surface Temperature, MASTER, Landsat-8, Calibration, Anisotropy

*Corresponding author

Email addresses: julien.michel@cnes.fr (Julien Michel), olivier.hagolle@cnes.fr (Olivier Hagolle), simon.j.hook@jpl.nasa.gov (Simon J. Hook), jean-louis.roujean@univ-tlse3.fr (Jean-Louis Roujean), philippe.gamet@cnes.fr (Philippe Gamet)

Preprint submitted to Remote Sensing of Environment June 22, 2023

8 **1. Introduction**

9 Earth observation from satellites provide radiometric data in the Thermal InfraRed
10 (TIR) spectrum, namely in the 8-12 μm range, that further serve to estimate the Land
11 Surface Temperature (LST), which is an Essential Climate Variable (ECV). LST is
12 used in a broad range of applications, notably to estimate the surface energy balance
13 (Anderson et al., 2008), and the evapo-transpiration (ET) (Price, 1982; Courault et al.,
14 2005; Anderson et al., 2012), allowing to detect plant water stress (Boulet et al., 2015)
15 and to monitor irrigation (Ishimwe et al., 2014).

16 A new generation of TIR sensors is foreseen to be launched in the coming years.
17 They will have a high spatial resolution (ground sampling distance close to 60 meters
18 at Nadir), and enhanced temporal resolution (every 3 days at equator, and even less at
19 higher latitudes), and between 4 and 5 TIR channels, as well as other optical channels.
20 Table 1 displays the main characteristics of these missions. The first on the agenda is
21 TRISHNA (Thermal infraRed Imaging Satellite for High-resolution Natural resource
22 Assessment) (Lagouarde et al., 2018), scheduled to be launched in 2026. This is a
23 joint Indian and French mission developed by ISRO and CNES. It should be followed
24 in 2027 by the Surface Biology and Geology (SBG) (Cawse-Nicholson et al., 2021),
25 which is a joint mission between NASA and the Italian Space Agency (ASI). Last, the
26 Land Surface Temperature Mission (LSTM) (Koetz et al., 2018) from the European
27 Space Agency will be launched in 2029 for the first satellite and 2030 for the second
28 one. All sensors from these TIR missions will be equipped with large Fields of View
29 (FOV), in order to achieve both global coverage and short revisit time.

30 With maximum zenith angles reaching 30 to 40 degrees, it is expected that direc-
31 tional effects will affect the thermal images and the retrieval of LST by several Kelvins.
32 They could therefore jeopardize the detection and monitoring of water stress as well
33 as other downstream products (Mwangi et al., 2022). A normalization effort seems
34 mandatory in order to reach the target accuracy of 1K for LST. For instance, the hotspot
35 phenomena later introduced in section 1.1 will frequently contaminate TRISHNA, SBG
36 and LSTM scenes in the tropics due to their overpassing time at noon. It is worth em-
37 phasizing that thanks to its orbit design, TRISHNA will provide a workaround to this

38 problem by observing the same scene with at least 3 different viewing angles within
 39 8 days, whereas SBG and LSTM have opted for constant angles. In all cases, pre-
 40 processing of the Level 2 products should benefit from a correction of the directional
 41 effects. It is noteworthy that even if viewing angles of a single are constant for a given
 42 location, directional effects correction may still be required for the joint use of data
 43 from the three missions.

Satellite	Status	Agencies	Launch	Resolution	Revisit	FoV
ASTER	End of life	JAXA	1999	90 .	16 days	8.55°
Landsat-8 & 9	Flying	NASA	2013/21	100 m	8d (2 sat)	7.5°
ECOSTRESS		NASA	2018	38x69 m	irregular	28°
TRISHNA	In prep.	CNES & ISRO	2025	57 m	3d (1 sat)	34°
SBG		NASA	2027	60 m	<8d (1 sat)	34°
LSTM		ESA	2029/31	37 m	2d (2 sat)	28°

Table 1: Main features of high resolution TIR satellites. For missions with two satellites (2 sat), both launch years are mentioned.

44 1.1. Directional anisotropy in the TIR domain

45 Satellite measurements of the LST inherently averages the temperature of visible
 46 elements within a pixel (Li et al., 2013). TIR directional effects are induced by changes
 47 in the proportions of those elements, within a pixel observed from different viewing an-
 48 gles. In structured landscapes, those elements can be divided into sunlit elements and
 49 shaded elements: when the sun and viewing directions get closer, proportion of visible
 50 shaded elements decreases, resulting in a larger proportion of hotter sunlit elements be-
 51 ing observed. This artificially increases the observed temperature, forming the hotspot
 52 phenomenon (Jupp and Strahler, 1991). Another effect inducing TIR anisotropy is the
 53 gap fraction (Nilson, 1999), resulting from the change in proportions of elements with
 54 different emissivities, and thus different temperatures, under the same solar radiation.
 55 For instance, when observing a cropland, observations with large viewing angles will
 56 increase the proportion of vegetation observed, while at nadir, the proportion of soil ob-
 57 served will be higher. In general, for vegetation pixels such as canopies or croplands,

58 the gap fraction and hotspot effects result from the continuous change of proportions
59 of sunlit and shaded leaves and sunlit and shaded background elements. More struc-
60 tured landscapes such as rows in croplands can emphasise both the hotspot and gap
61 fraction effects, depending on the row orientation with respect to the satellite azimuth
62 (Lagouarde et al., 2014). Finally, It is noteworthy that directional effects may also
63 affect the Land Surface Emissivity (LSE) (Sobrino and Cuenca, 1999; Ermida et al.,
64 2020).

65 Directional effects in the reflective domain have been well studied (Roujean et al.,
66 1992; Wanner et al., 1995; Roujean, 2000) and model-based corrections are routinely
67 applied to high resolution imagery such as Landsat and Sentinel-2 (Claverie et al.,
68 2018). Directional effects in TIR domain were primarily investigated by means of
69 simulations (Duffour et al., 2016; Cao et al., 2019; Bian et al., 2020, 2023) using
70 physically-based radiative transfer codes such as 1D SCOPE (Yang et al., 2021) and 3D
71 DART (Gastellu-Etchegorry, 1996; Gastellu-Etchegorry et al., 2017). Detailed DART
72 mock-ups were built for various land-cover types. Parametric models (Ermida et al.,
73 2018; Cao et al., 2021), are considered as the only mean to routinely correct for direc-
74 tional effects, and thereby be used in the ground segments processors. They were eval-
75 uated against SCOPE and DART simulations (Pinheiro et al., 2006; Bian et al., 2018;
76 Cao et al., 2019), or by cross-comparison with field measurements (Duffour et al., 2016)
77 and medium resolution LEO (Low Elevation Orbit) and GEO (geostationary) satellites
78 with large FOVs (Vinnikov et al., 2012; Guillevic et al., 2013; Ren et al., 2014).

79 Current operating TIR High-Resolution (HR, 10 meter to 100 meter) satellite im-
80 agery is acquired by instruments with a narrow FOV, such as Landsat-8 ($\pm 7.5^\circ$) or
81 ASTER ($\pm 8.5^\circ$), where directional effects do not have a significant impact on LST
82 measurements. A noticeable exception is the ECOSTRESS mission flying onboard the
83 International Space Station (ISS) (Fisher et al., 2020), with its wide FOV ($\pm 30^\circ$).
84 Currently, there is no systematic correction of directional effects in the level 2 data
85 processing of ECOSTRESS (Hulley and Hook, 2018).

86 *1.2. Main contributions*

87 Simulating directional effects is valuable to understand the underlying physics, and
88 to evaluate parametric models in a controlled environment. Simulations however have
89 a limited variability with respect to the natural landscape that will be observed by a
90 global coverage satellite mission. Databases of in situ measurements also lack suffi-
91 cient diversity as they focus on a few plant species and land-cover types over selected
92 geographic areas. Lower resolution (larger area) pixels from LEO and GEO satellites
93 TIR images are a good complement to theoretical studies and field campaigns but their
94 large pixels may include different types of landscapes whereas forthcoming higher res-
95 olution TIR missions will focus on a finer scale.

96 This work aims to assess a directional error budget in preparation of up-coming
97 high spatial resolution TIR missions by utilizing available Landsat-8 imagery (Roy
98 et al., 2014) combined with near simultaneous observations from the MODIS/ASTER
99 airborne simulator (MASTER) (Hook et al., 2001). Evidences of directional behavior
100 are identified and compared to several well-established directional models from the
101 literature.

102 Landsat-8 is the well-known Earth-observation satellite from the Landsat series,
103 providing a global coverage of the globe with a 16-days revisit since 2013. Landsat-8
104 has a TIR sensor resolution of 100 meters, though level 1 and 2 products further inter-
105 polate LST products to 30 meters. The Landsat-8 FOV is quite narrow, as its maximum
106 View Zenith Angle (VZA) is 7.5° , and LST maps will therefore be considered as ac-
107 quired under near Nadir conditions in this study. MASTER is an airborne sensor jointly
108 developed by Ames Research Center (ARC), Jet Propulsion Laboratory (JPL), and the
109 EROS Data Center to support algorithms development, calibration and validation for
110 the ASTER and MODIS teams. The MASTER instrument has 50 channels in the 0.4
111 - 13 μm range, with 10 bands in the TIR wavelength range, with a large FOV (maxi-
112 mum VZA of 42.5°). It has been regularly flown since 1998, providing more than 658
113 days of acquisition. Spatial resolution ranges from 5 meters to 50 meters depending
114 on the aircraft flight altitude. While Landsat-8 can provide near Nadir observations,
115 MASTER fully covers the spatial resolution and VZA of the up-coming HR TIR mis-
116 sions listed in table 1. Though ECOSTRESS could also be considered, its FOV (28°)

117 does not cover the full FOV of the up-coming missions. Moreover, ECOSTRESS has
118 a very large swath, and a single Landsat-8 scene only covers a fraction of the VZAs of
119 ECOSTRESS. MASTER being an airborne sensor, it covers the full range of VZA in a
120 very narrow swath that fits completely into a Landsat-8 image.

121 The remainder of this paper is organised as follows. Section 2 presents the matching
122 methodology, the data processing, as well as the directional models and models fitting
123 procedure. Section 3 presents LST comparison statistics for each match, the evidences
124 of the directional effects and the performances of directional models fitted on the data.
125 Section 4 discusses the limitations and possible follow-up to this study, and section 5
126 summarizes the results and future work.

127 **2. Materials and methods**

128 *2.1. Matching methodology*

129 The full MASTER archive metadata has been kindly provided by JPL, and Landsat-
130 8 collection 2 level 2 archive metadata (as of 2022.02.17) has been downloaded from
131 the Land Processes DAAC. From these data, all pairs of MASTER and Landsat-8 prod-
132 ucts acquired during day-time, on the same date, with acquisition times within 10 min-
133 utes of each other, and with an overlap of respective bounding boxes no less than 50%
134 have been selected.

135 Using this search process, 52 matches were identified, for which the Landsat-8
136 overpass occurs during MASTER track flight. Those 52 matches correspond to 24
137 unique MASTER tracks since one track can correspond to two Landsat-8 product.
138 Among those 52 matches, 7 MASTER tracks are missing in the archive, which invali-
139 dates 17 pairs. This leaves 35 pairs for which both Landsat-8 products and MASTER
140 L1B (radiance at sensor) and L2 (derived LST and emissivities) products are available.
141 Among those, there are 16 pairs for which the processing described in section 2.2 does
142 not yield a valid difference image, because of cloud occurrences or insufficient swath
143 final overlap. Table 2 gives the products references of all valid pairs used in this study.
144 As shown in figure 1, all sites are located in California or nearby. Figure 2 shows a
145 detailed map view of valid overlapping area for each MASTER track, with the overlap

146 of the second Landsat-8 image in blue when applicable. This map shows that for most
 147 of the tracks (3, 4, 6, 10, 12), the second Landsat-8 does not bring additional coverage,
 148 to the noticeable exception of tracks 8 and 9.

Id	MASTER track id	Landsat L2 product id
1	2013-03-29_18:06:53	LC08_L2SP_038037_20130329_20200912_02_T1
2	2013-04-11_18:14:46	LC08_L2SP_041036_20130411_20200912_02_T1
3a	2013-05-22_18:13:09	LC08_L2SP_040036_20130522_20200913_02_T1
3b	2013-05-22_18:13:09	LC08_L2SP_040037_20130522_20200913_02_T1
4	2013-12-05_18:23:35	LC08_L2SP_043035_20131205_20200912_02_T1
5a	2014-03-31_18:11:16	LC08_L2SP_039035_20140331_20200911_02_T1
5b	2014-03-31_18:11:16	LC08_L2SP_039036_20140331_20200911_02_T1
6a	2014-04-14_18:27:14	LC08_L2SP_041036_20140414_20200911_02_T1
6b	2014-04-14_18:27:14	LC08_L2SP_041037_20140414_20200911_02_T1
7	2014-04-28_18:22:43	LC08_L2SP_043035_20140428_20200911_02_T1
8a	2014-06-06_18:25:35	LC08_L2SP_044033_20140606_20200911_02_T1
8b	2014-06-06_18:25:35	LC08_L2SP_044034_20140606_20200911_02_T1
9a	2014-10-21_18:35:15	LC08_L2SP_043034_20141021_20200910_02_T1
9b	2014-10-21_18:35:15	LC08_L2SP_043035_20141021_20200911_02_T1
10a	2015-05-28_18:13:05	LC08_L2SP_040036_20150528_20200909_02_T1
10b	2015-05-28_18:13:05	LC08_L2SP_040037_20150528_20200909_02_T1
11	2018-06-19_18:28:30	LC08_L2SP_042034_20180619_20200831_02_T1
12a	2021-03-30_18:32:40	LC08_L2SP_043033_20210330_20210409_02_T1
12b	2021-03-30_18:32:40	LC08_L2SP_043034_20210330_20210409_02_T1

Table 2: List of valid MASTER and Landsat-8 pairs

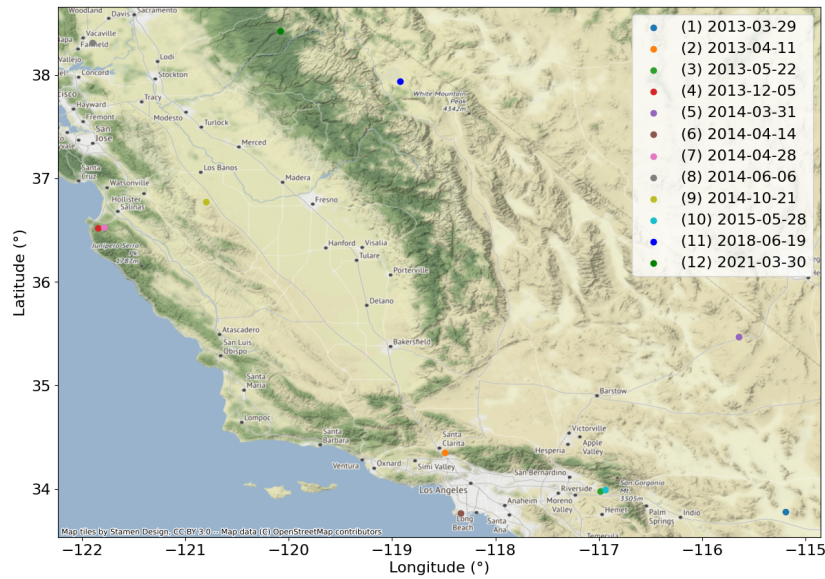


Figure 1: Location of the 12 MASTER tracks that have been matched to near simultaneous Landsat-8 acquisitions

149 **2.2. Data Processing**

150 **2.2.1. Product downloads**

151 Landsat-8 products have been downloaded from the collection 2 level 2 archive
 152 from the EarthExplorer portal¹. MASTER L1B products (radiances and viewing an-
 153 gles), as well as L2 products (LST and geo-location grids) have been requested on
 154 the MASTER website². Landsat-8 viewing angles have been computed by using a C
 155 program publicly available on USGS website³.

156 **2.2.2. Target variables**

157 *Surface Brightness Temperature (SBT)*. Both mission output LST and LSE maps. But
 158 they differ in the way those variables are estimated. On Landsat-8, there is a single

¹<https://earthexplorer.usgs.gov/>, consulted on 2023.03.01

²<https://masterprojects.jpl.nasa.gov/>, consulted on 2023.03.01

³<https://www.usgs.gov/landsat-missions/solar-illumination-and-sensor-viewing-angle-coefficient-file>,
 consulted on 2022.09.12

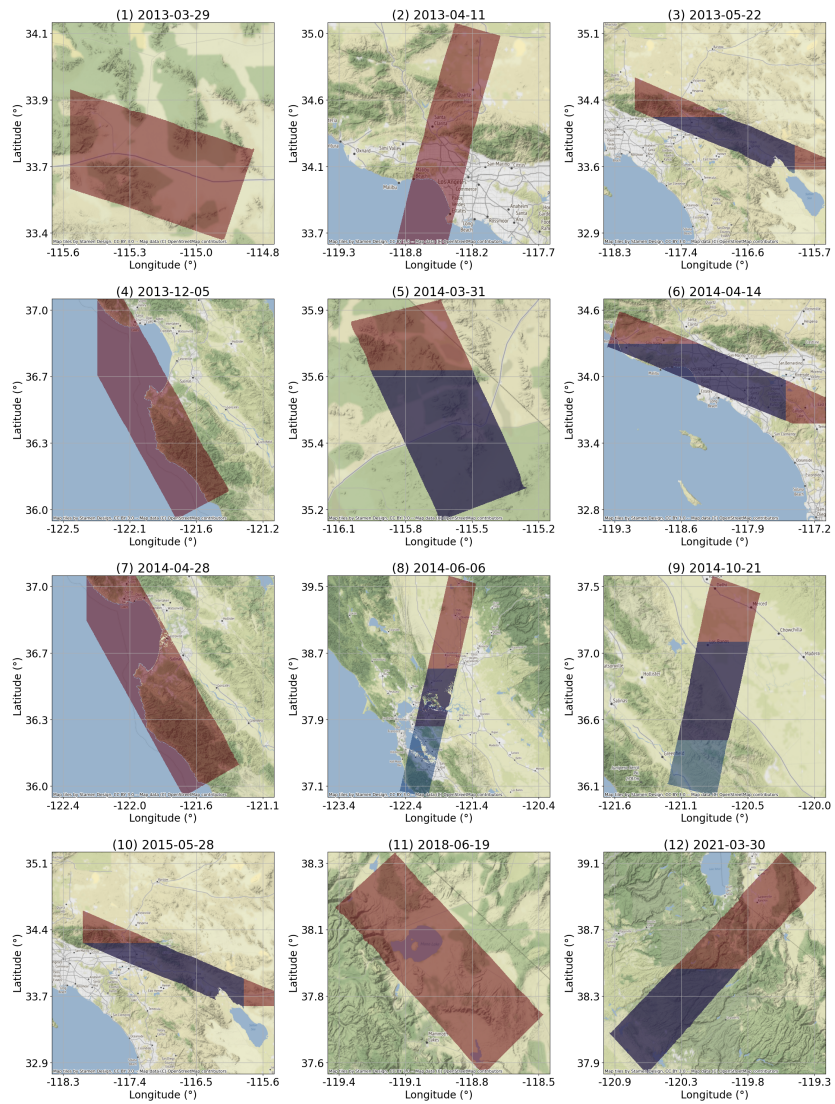


Figure 2: Detailed view of the overlapping MASTER tracks and Landsat-8 near simultaneous acquisitions. When two Landsat-8 images match a given track, the first image (a) is displayed in red and second image (b) in blue.

159 usable TIR band (B10, 10.6 - 11.19 μm), which prevents a joint estimation of LST and
 160 LSE. LSE is therefore derived by modulating the LSE from the ASTER Global Emis-
 161 sivity Database (Hulley et al., 2015) with the Normalized Difference Index (NDVI) and
 162 Snow Difference Index (NDSI) measured by Landsat-8. Various rules are applied to
 163 clamp emissivity values in corner cases. One important thing to note is that any emis-
 164 sivity lower than 0.6 is considered invalid and flagged as missing data. LST is then
 165 obtained by inverting the radiative transfer equation 1, with the atmospheric transmit-
 166 tance, upwelled and downwelled radiance estimated using (MODerate resolution atmo-
 167 spheric TRANsmission (MODTRAN) (Berk et al., 2014), Modern-Era Retrospective
 168 analysis for Research and Applications, Version 2 (MERRA-2) (Gelaro et al., 2017)
 169 and data from the GEOS-5 FP-IT Atmospheric Data Assimilation System (GEOS-5
 170 ADAS) (Malakar et al., 2018).

$$L_\lambda(\theta) = [\epsilon_\lambda B_\lambda(T_s) + (1 - \epsilon_\lambda)L_\lambda^\downarrow]\tau_\lambda(\theta) + L_\lambda^\uparrow(\theta) \quad (1)$$

171 where $L_\lambda(\theta)$ is the at sensor radiance, λ is the wavelength, θ is the observation angle,
 172 ϵ_λ the surface emissivity, T_s is the Surface Temperature, L_λ^\downarrow is the downwelled radiance,
 173 $\tau_\lambda(\theta)$ is the atmospheric transmittance, $L_\lambda^\uparrow(\theta)$ is the upwelled radiance and $B_\lambda(T_s)$ is the
 174 Planck function defined in equation 2.

$$B_\lambda(T_s) = \frac{2hc^2}{\pi\lambda^5 \left(\exp\left(\frac{hc}{\lambda T_s}\right) - 1 \right)} = \frac{C_1}{\lambda^5 \left(\exp\left(\frac{C_2}{\lambda T_s}\right) - 1 \right)} \quad (2)$$

175 Where $h = 6.63 \times 10^{-34} \text{Ws}^2$ (Planck constant), $c = 2.99 \times 10^8 \text{ms}^{-1}$ (speed of light),
 176 $k = 1.38 \times 10^{-23} \text{WsK}^{-1}$ (Boltzmann constant), $C_1 = 2\pi hc^2 = 3.74 \times 10^{-16} \text{Wm}^2$ (first
 177 radiative constant) and $C_2 = hc/k = 1.44 \times 10^4 \mu\text{mK}$ (second radiative constant).

178 MASTER, on the other hand, uses the ASTER TES algorithm to retrieve LST val-
 179 ues (Hook et al., 2011), using MODTRAN radiative transfer code and atmospheric
 180 parameters the Global Data Assimilation System (GDAS) products from the National
 181 Center for Environmental Prediction (NCEP). Those parameters are optimized for a
 182 flight altitude of 20 kilometers. Level 2 products include LST estimates as well emis-
 183 sivity estimates for channels 43, 44, 47, 48 and 49.

184 Since the algorithms for the separation of emissivity and LST are different, those

185 two variables may exhibit differences that are not related to directional effects. In order
 186 to limit the impact of those differences, this study recomputes the Surface Brightness
 187 Temperature (SBT), which corresponds to the temperature of a black-body emitting the
 188 same surface radiance, for both sensors, by means of equation 3, where $\lambda = 10.9\mu m$
 189 (center wavelength of Landsat-8 B10 band).

$$SBT = B_{\lambda}^{-1}(emis * B_{\lambda}(LST)) \quad (3)$$

190 Note that equation 3 is only changing the balance between already estimated emis-
 191 sivities and LST, under the same radiative transfer budget.

Equivalent Landsat-8 emissivity from MASTER. MASTER channels 47 and 48 overlap Landsat-8 B10 spectral sensitivity response, as shown in figure 3. Since the overlaps are significant, an equivalent Landsat-8 B10 emissivity is derived from MASTER, by means of linear combination of emissivities of channel 47 and 48, as shown in equation 4 to 6. The weights of the linear combinations are derived from the integration of the product of spectral sensitivities response, which correspond to the green and orange areas in figure 3. Weights are given in equation 7. This equivalent emissivity will be used as the MASTER emissivity throughout this study.

$$\epsilon^* = \frac{w_{47}}{w_{47} + w_{48}} \epsilon_{47} + \frac{w_{48}}{w_{47} + w_{48}} \epsilon_{48} \quad (4)$$

$$w_{47} = \int_{\lambda} SRS_{B10}^{landsat-8}(\lambda) * SRS_{47}^{MASTER}(\lambda) \quad (5)$$

$$w_{48} = \int_{\lambda} SRS_{B10}^{landsat-8}(\lambda) * SRS_{48}^{MASTER}(\lambda) \quad (6)$$

192

$$\frac{w_{47}}{w_{47} + w_{48}} = 0.605, \quad \frac{w_{48}}{w_{47} + w_{48}} = 0.395 \quad (7)$$

193 2.2.3. Geometric processing

194 In order to compare measurements from products from the different sensors, they
 195 need to be first resampled to a common cartographic sampling grid. For each pair, this
 196 grid is defined using the Universal Transverse Mercator (UTM) cartographic projection
 197 of the Landsat-8 image of the pair. The sampling grid is defined according to the
 198 overlap area of the two products, and aligned to a multiple of the target resolution. The

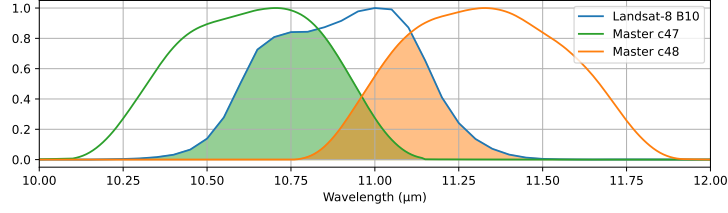


Figure 3: Spectral Sensitivity Response of Landsat-8 and MASTER overlapping Thermal Infra-Red spectral bands

199 target resolution is set to 100 meters for pairs of Landsat-8 and MASTER images, since
 200 the native resolution of Landsat-8 TIR bands is 100 meter.

201 Landsat-8 resampling is achieved through an averaging filter, which should not
 202 incur any aliasing artifacts since the Landsat-8 LST and emissivity measurements are
 203 resampled at 30 meters resolution through bicubic interpolation. MASTER being a
 204 whisk-broom sensor, its sampling is regular in viewing angle and therefore irregular in
 205 ground geometry: both spacing between pixels and pixel size increase with the viewing
 206 angle. Resampling of those measurements to the target ground grid is achieved by
 207 means of Gaussian Weights Averaging (GWA), as described in equation 8, through its
 208 implementation in the *pyresample* library (Hoese et al., 2022):

$$V(x, y) = \sum_{i \in N(x, y)} e^{-\frac{(x-x_i)^2 + (y-y_i)^2}{\sigma^2}} V_i \quad (8)$$

209 Where (V_i, x_i, y_i) are swath samples of measurement V at location (x_i, y_i) , $N(x, y)$
 210 are the N nearest neighbours of target ground location (x, y) , and σ is a user-defined
 211 parameter, which is set using equation 9:

$$\sigma(r, R, mtf) = \frac{\max(r, R)}{\pi} \sqrt{-2 \ln(mtf)} \quad (9)$$

212 Where mtf is the value of the Modulation Transfer Function (MTF) at Nyquist
 213 cut-off frequency, allowing to trade level of blur and aliasing off, r is the native sensor
 214 resolution and R is the target resolution. In this work, MTF has been set to 0.1, which
 215 yields a sigma of 68.3 meters for MASTER.

216 Given that all MASTER flights occurred at an altitude between 19 702 meters and
 217 20 088 meters, depending on the position in the swath and the flight azimuth, the output

218 100 meter pixels cover between 12.5 milliradians and 23.7 milliradians of the initial
 219 instantaneous MASTER FOV, which is 2.25 milliradians per pixel.

220 2.2.4. *Quality filtering*

221 Only samples that are marked as clear and not flagged as water or snow in the Pixel
 222 Quality Assessment mask from the Level 2 Landsat-8 products are kept for analysis.
 223 No additional quality filtering is performed on the MASTER side.

224 2.2.5. *Angular distance*

225 Let (θ_0, ϕ_0) and (θ_1, ϕ_1) denote two viewing directions by their zenith angle θ and
 226 azimuth angle ϕ . The angle between those two viewing directions is given by equation
 227 10:

$$D_{ang}(\theta_0, \phi_0, \theta_1, \phi_1) = \arccos(\sin(\theta_0) \times \sin(\theta_1) \times \cos(\phi_0 - \phi_1) + \cos(\theta_0) \times \cos(\theta_1)) \quad (10)$$

228 This distance is used in this work to measure proximity to hotspot conditions, as
 229 well as to measure distance between MASTER and Landsat-8 viewing directions.

230 2.3. *Directional parametric models*

231 Four models investigated by [Cao et al. \(2019\)](#) have been used in this work: the
 232 Ross-Li model ([Roujean et al., 1992](#); [Wanner et al., 1995](#); [Ren et al., 2014](#)), the LSF-Li
 233 model ([Su et al., 2002](#)), the Vinnikov model ([Vinnikov et al., 2012](#)) and the RL model
 234 ([Roujean, 2000](#); [Lagouarde and Irvine, 2008](#)). In addition to those models, we also
 235 investigated the LSF-RL model from [Cao et al. \(2021\)](#). Models are presented in table 3,
 236 where θ_v (resp. θ_s) is the view (resp. solar) zenith angle, and Δ_ϕ denotes the difference
 237 between solar and view azimuth angle. Unless stated otherwise, remaining notations
 238 and kernel expressions will be those from [Cao et al. \(2019\)](#). The full kernel functions
 239 are not provided here for the sake of conciseness. All models m will be expressed as
 240 stated in equation 11, with k_0, \dots, k_n being the free parameters of the model:

$$T(\theta_v, \theta_s, \Delta_\phi) = m(\theta_v, \theta_s, \Delta_\phi, k_0, \dots, k_n) \times T_{Nadir} \quad (11)$$

241 For the sake of consistency with the other models, the Roujean-Lagouarde (RL)
 242 kernel has been rewritten as equation 12:

$$K_{RL}(\theta_v, \theta_s, k_{hs}) = \frac{e^{-k_{hs}f} - e^{-k_{hs}f_n}}{1 - e^{-k_{hs}f_n}} \quad (12)$$

243 with f and f_n as written in Cao et al. (2019) (eq. 13 and 14). This mainly moves
 244 the original Δ_T parameter out of the kernel formulation, in order to use it as a kernel
 245 coefficient in table 3. It must be stressed that the RL model is the only one that does
 246 not have a volumetric kernel, but only a geometric kernel. The LSF-RL complement
 247 the RL model with the LSF volumetric kernel. To make that more obvious, in table 3,
 248 the parameter k_0 always represents the isotropic contribution, while k_1 stands for the
 249 coefficient of the volumetric kernel (and therefore the RL model has no k_1 parameter),
 250 and k_2 is the coefficient of the geometric or hotspot kernel. The hotspot width parameter
 251 inside the exponential in 12 is labelled k_{hs} , and it should be noted that the RL and LSF-
 252 RL models are the only models with parameters non-linearity.

Model	Iso	Volumetric	Geometric / Hotspot
Ross-Li	k_0	$+ k_1 \mathbf{K}_{\text{RossThick}}(\theta_v, \theta_s, \Delta_{\text{phi}})$	$+ k_2 \mathbf{K}_{\text{LiSparseR}}(\theta_v, \theta_s, \Delta_{\text{phi}})$
LSF-Li	k_0	$+ k_1 \mathbf{K}_{\text{lsf}}(\theta_v, \theta_s, \Delta_{\text{phi}})$	$+ k_2 \mathbf{K}_{\text{LiDenseR}}(\theta_v, \theta_s, \Delta_{\text{phi}})$
Vinnikov	k_0	$+ k_1 \mathbf{K}_{\text{emis}}(\theta_v, \theta_s, \Delta_{\text{phi}})$	$+ k_2 \mathbf{K}_{\text{solar}}(\theta_v, \theta_s, \Delta_{\text{phi}})$
RL	k_0		$+ k_2 \mathbf{K}_{\text{RL}}(\theta_v, \theta_s, \Delta_{\text{phi}}, k_{hs})$
LSF-RL	k_0	$+ k_1 \mathbf{K}_{\text{lsf}}(\theta_v, \theta_s, \Delta_{\text{phi}})$	$+ k_2 \mathbf{K}_{\text{RL}}(\theta_v, \theta_s, \Delta_{\text{phi}}, k_{hs})$

Table 3: Formulations of the five directional models from Cao et al. (2019) as well as of the LSF-RL model from Cao et al. (2021) investigated in this work

253 The fitting of model parameters on the data has been performed by ordinary Least-
 254 Squares as stated in equation 13:

$$\min_{(k_0, k_1, k_2, k_{hs})} \| m(\theta_v, \theta_s, \Delta_{\text{phi}}, k_0, \dots, k_{hs}) \times T_{\text{Nadir}} - T_{\text{Dir}}(\theta_v, \theta_s, \Delta_{\phi}) \|^2 \quad (13)$$

255 where Landsat-8 SBT is used as T_{Nadir} and MASTER SBT is used as T_{Dir} . Pa-
 256 rameters k_0 , k_2 and k_{hs} are assumed to be strictly positive, and in Cao et al. (2019)
 257 the authors observe that k_1 is always negative. Additionally, k_{hs} can not equal 0 in or-

258 der to avoid a null denominator in the exponential fraction. In order to enforce those
 259 constraints while still using unconstrained least-squares fitting, the models have been
 260 re-parametrized with exponential, and a small offset of 1e-6 has been added to k_{hs} to
 261 avoid the under-determination around 0, as shown in equation 14:

$$k_0 = e^{k'_0}, \quad k_1 = -e^{k'_1}, \quad k_2 = e^{k'_2}, \quad k_{hs} = 1e - 6 + e^{k'_{hs}} \quad (14)$$

262 Optimization has been performed using the Levenberg-Marquardt algorithm imple-
 263 mented in scipy (Virtanen et al., 2020). Initial values have been set to 1. for k_0 , 0.01
 264 for k_1 and k_2 , which corresponds to a variation of SBT of 1% that is consistent with the
 265 observations in the dataset, and 1 for k_{hs} , where k_0 , k_1 , k_2 and k_{hs} defined in table 3.

266 2.4. Land-cover analysis

267 According to the literature, Land cover is one of the main drivers for TIR direc-
 268 tional anisotropy, as both gap fraction and hotspot effects are driven by the structure of
 269 the landscape, and in particular, of the vegetation. In order to provide insights on the
 270 land-cover classes covered by each of the tracks, five high level classes have been ex-
 271 tracted from the Copernicus Global Land Service maps at 100 meter resolution (Tsend-
 272 bazar et al., 2021). This land cover source has been selected because it is available as
 273 open-data, it covers the area of interest and provides several years of land cover maps
 274 covering the observation period. Maps from Copernicus GLS only cover years 2015
 275 to 2019, whereas MASTER tracks cover years 2013 to 2021, therefore tracks prior to
 276 2015 have been assigned the 2015 land cover, while tracks posterior to 2019 have been
 277 assigned the 2021 land cover, under the assumption that land cover only marginally
 278 changes from one year to another, especially for high level classes. High level classes
 279 are aggregated from the land-cover maps as described in table 4. Furthermore, since
 280 vegetation can be at different stages of growth depending on plant type and season, the
 281 cropland, low vegetation and forests classes have been further stratified according to
 282 the Normalized Difference Vegetation Index (NDVI) (Kriegler et al., 1969) computed
 283 from Landsat-8 in three sub-classes : low NDVI (between 0 and 0.2), intermediate
 284 NDVI (between 0.2 and 0.6), and high NDVI (greater than 0.6).

High level class	Copernicus Global Land Service classes (label)
Urban	Urban / built up (50)
Bare	Bare / sparse vegetation (60)
Croplands	Cultivated and managed vegetation/agriculture (cropland) (40)
Low vegetation	Shrubs (20)
	Herbaceous vegetation (30)
	Herbaceous wetland (90)
	Moss and lichen (100)
Forests	Closed forest, evergreen needle leaf (111)
	Closed forest, evergreen, broad leaf (112)
	Closed forest, deciduous needle leaf (113)
	Closed forest, deciduous broad leaf (114)
	Closed forest, mixed (115)
	Closed forest, unknown (116)
	Open forest, evergreen needle leaf (121)
	Open forest, evergreen broad leaf (122)
	Open forest, deciduous needle leaf (123)
	Open forest, deciduous broad leaf (124)
	Open forest, mixed (125)
	Open forest, unknown (126)

Table 4: The five high level class derived from class aggregation of the Copernicus Global Land Service classes

285 Table 5 gives the proportions of each classes for each analysed MASTER track.
 286 All proportions are given in percentage of the total number of available pixels. In this
 287 table, it can be noted that low vegetation and croplands seldom reach the highest NDVI
 288 strata, while forests have intermediate to high NDVI, which is expected and advocate
 289 for the consistency between the derived land-cover maps and the observed landscapes.
 290 Track (1) is mostly composed of bare soil. Tracks (8) and (9) are the only ones with
 291 a significant proportion of croplands, all in the intermediate NDVI strata. Tracks (2)
 292 and (6) are the only ones with a significant proportion of urban pixels, and are com-
 293 plemented with low to intermediate NDVI classes of low vegetation. Remaining tracks
 294 are a mix of forests with intermediate to high NDVI, and low vegetation with low to
 295 intermediate NDVI.

ndvi	bare	urban	crops			forests			low veg.		
			low	inter	high	low	inter	high	low	inter	high
(1)	80.9	0.1	0.0	0.0	0.0	0.0	0.0	0.0	18.6	0.3	0.0
(2)	1.9	25.2	0.1	0.1	0.1	0.0	3.1	3.0	34.1	29.2	3.2
(3)	16.0	11.9	0.0	0.0	0.0	0.1	15.7	8.6	20.0	26.4	1.1
(4)	0.1	3.9	0.0	0.1	0.0	0.3	26.8	56.8	0.5	9.9	1.4
(5)	17.5	0.0	0.0	0.1	0.2	0.0	0.7	0.0	73.9	7.5	0.0
(6)	0.8	51.0	0.2	2.4	1.0	0.1	5.0	4.8	1.9	29.0	3.8
(7)	0.1	3.1	0.3	3.4	1.5	0.0	15.5	57.0	0.2	13.2	5.4
(8)	0.2	13.4	4.0	28.3	8.7	0.1	10.9	14.4	1.3	17.5	0.7
(9)	0.0	2.2	9.0	26.3	4.3	0.0	6.1	0.8	18.2	32.9	0.1
(10)	20.6	14.5	0.0	0.1	0.0	0.1	13.5	4.7	20.4	25.4	0.6
(11)	14.5	0.0	0.0	0.0	0.0	0.5	23.2	0.9	18.9	39.6	2.3
(12)	0.9	1.0	0.1	0.9	0.3	1.9	28.9	33.4	12.8	14.5	5.2

Table 5: Percentage of land-cover classes for each track. Vegetation classes are further stratified according to Landsat-8 NDVI into [0,0.2] (low), [0.2,0.6] (intermediate) and [0.6, 1.0] (high). Classes exceeding 15% of available pixels are highlighted in bold for the sake of readability.

296 **3. Results**

297 *3.1. SBT difference analysis*

298 Table 6 shows the biases and RMSE of LST and SBT differences (Landsat-8 -
299 MASTER), for each MASTER track, and for samples for which angles between view-
300 ing directions are below 7° . Though each track exhibits an absolute LST bias lower
301 than 1.8 K (1.6 K for SBT), the biases of each track vary significantly within this range.
302 Standard deviation values range from 0.7 K to up to 2.2 K for LST and 0.6K to 2K for
303 SBT, if we exclude track (10) which exhibits a very large standard deviation. Those
304 values are in line with recent Landsat-8 LST performance assessment for Landsat-8
305 Collection 2 Level 2 (Niçlòs et al., 2021). For all tracks, SBT standard deviation is
306 lower than LST standard deviation. SBT is therefore more suitable for the analysis in
307 this paper, as it seems to discard discrepancies related to the different LST - emissivity
308 separation methods detailed in section 2.2.2. In order to further reduce discrepancies
309 unrelated to directional anisotropy, on each track SBT differences will be corrected
310 from the bias, so that similar viewing angles between MASTER and Landsat-8 corre-
311 spond to a null SBT difference on average. It is noteworthy that standard deviation in
312 table 6 corresponds to the Root Mean Squared Error (RMSE) of the de-biased data.

313 Figure 4 shows the SBT difference maps for each track, which have been corrected
314 from the biases shown in table 6. Most tracks exhibit a pattern related to the position
315 in the MASTER swath, and thus to the MASTER VZA. This is for instance the case
316 form tracks (2), (6), (7), (8) and (12), where MASTER SBT appears to be consistently
317 warmer on the western side of the swath than on the eastern side of the swath. Tracks
318 (4), (9) and (10) have the highest SBT difference standard deviations in table 6 and ex-
319 hibit spatial patterns that seem uncorrelated to TIR anisotropy. Inspection of Landsat-8
320 cirrus band B9 in level 1C products from collection 2 reveals that track (10) is heavily
321 contaminated by unmasked cirrus clouds, which explains both its high SBT difference
322 standard deviation and large spatial patterns in SBT difference map. Likewise, a closer
323 inspection of track (4) reveals that the SBT difference map is completely dominated
324 by terrain effects, which explains both its high SBT difference standard-deviation and
325 noisy spatial patterns. Inspection of remaining tracks reveals that track (9) is also partly

Track	#samples	LST		SBT	
		Bias	Std dev	Bias	Std dev
(1) 2013-03-29	5187	-0.6	0.7	-0.7	0.6
(2) 2013-04-11	69125	0.3	1.4	0.6	1.3
(3) 2013-05-22	59011	1.4	1.6	1.1	1.5
(4) 2013-12-05	7409	0.7	1.9	0.4	1.9
(5) 2014-03-31	22037	1.2	1.0	0.9	0.6
(6) 2014-04-14	73182	0.4	1.2	0.2	1.1
(7) 2014-04-28	13012	0.6	1.0	1.0	1.0
(8) 2014-06-06	138921	-0.3	1.8	-0.1	1.7
(9) 2014-10-21	74247	-1.5	2.1	-1.5	2.1
(10) 2015-05-28	97435	-0.1	5.5	-0.3	5.4
(11) 2018-06-19	36706	-1.3	1.7	-1.6	1.6
(12) 2021-03-30	62572	-1.7	1.9	-1.1	1.7

Table 6: Bias and RMSE of Land Surface Temperature and SBT difference (Landsat-8 - MASTER) for samples with an absolute viewing angles distance below 7°

326 contaminated by unmasked cirrus clouds and terrain effects. Tracks (4), (9) and (10)
327 have therefore been excluded from the analysis in the remaining of this paper.

328 *3.2. Directional effects analysis*

329 *3.2.1. Distance to hotspot vs. distance to Landsat-8 viewing direction*

330 In figure 5, SBT differences, corrected from the biases shown in table 6, are anal-
331 ysed with respect to both MASTER view angular distance to hotspot and to Landsat-8
332 viewing direction. All graphs exhibit the same v-shaped curve, which is induced by the
333 relative viewing geometries between Landsat-8 and MASTER. Since Landsat-8 has a
334 narrow FOV, the minimum angular distance between views occurs far from the hotspot
335 condition (usually between 20° and 50° of distance to the hotspot), and with MASTER
336 view close to Nadir. On the left of the minimum point, which corresponds to the west-
337 ern part of the MASTER swath, the MASTER view gets closer to the hotspot, which
338 correlates with MASTER temperature getting hotter than Landsat-8 temperature. This
339 is especially visible for tracks (2), (8) and (12), which are also the tracks that come
340 closer to the hotspot. On the right of the minimum point, which corresponds to the
341 eastern part of the MASTER swath, the view gets away from the hotspot condition,
342 which correlates in most views with MASTER getting colder than Landsat-8.

343 *3.2.2. MASTER view zenith and azimuth*

344 Figure 6 allows to better understand the angular configurations of each MASTER
345 track with respect to the position of the sun. Two kinds of configurations can be ob-
346 served. In hotspot conditions, when the sun is close to the principal observation plane,
347 as in tracks (2), (8) and (12), the temperature steadily increases while coming closer to
348 the sun position. On track (8), MASTER view zenith gets higher than the sun zenith
349 which results in a cool-down of the SBT. Track (12) shows that the sun is almost in the
350 principal plane, which explains why this track has the smallest distance to the hotspot.
351 When the sun is far from the principal observation plane however, SBT gets colder
352 with higher view zenith angle, on both ends of the swath. The difference with Landsat-
353 8 SBT comes to a minimum near nadir, but the position of this minimum varies and

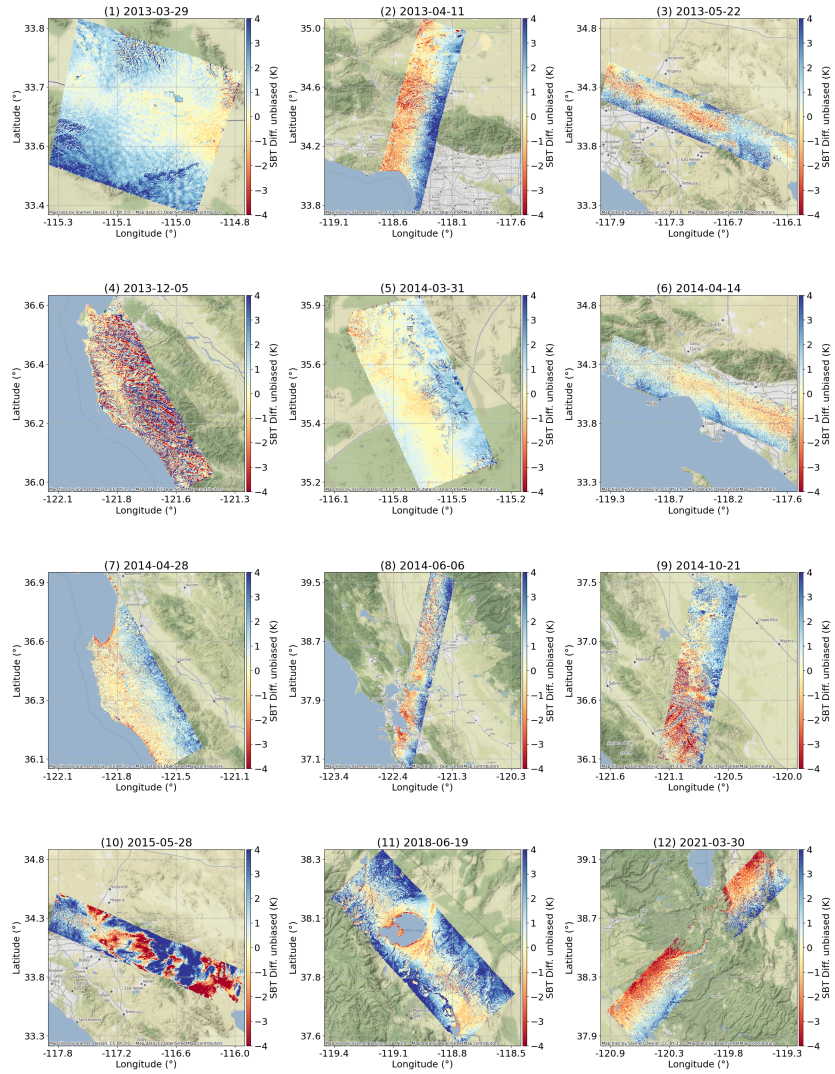


Figure 4: Maps of SBT difference (Landsat-8 - MASTER), corrected of the bias computed in table 6 for all tracks (negative values are in red and mean that MASTER is warmer than Landsat-8)

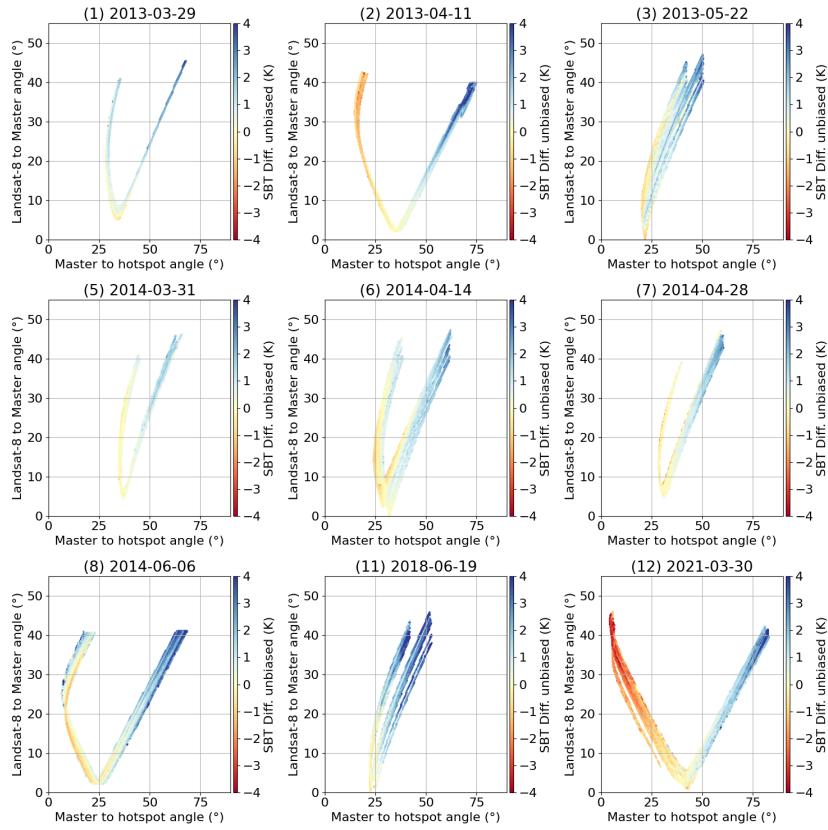


Figure 5: SBT difference (Landsat-8 - MASTER) with respect to angular distance from MASTER to hotspot and from MASTER to Landsat-8, corrected of the bias computed in table 6 (negative values are in red and mean that MASTER is warmer than Landsat-8)

354 seems to be influenced by the position of the sun. This may be related to gap fraction
 355 effect and can be observed on tracks (1), (3), (5), (6), (7) and (11).

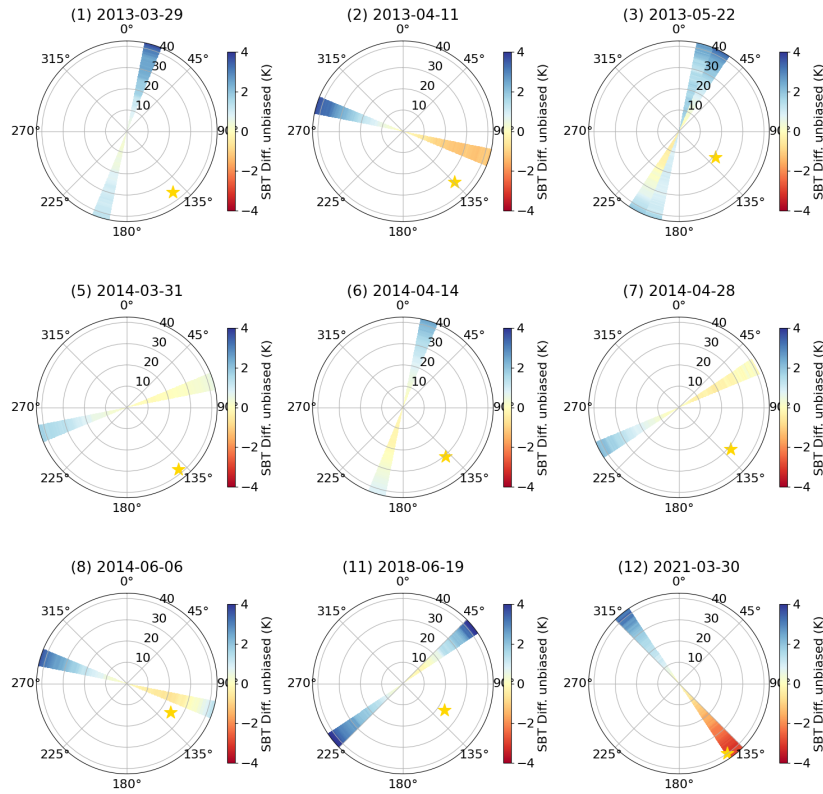


Figure 6: SBT difference (Landsat-8 - MASTER) with respect to MASTER view zenith and azimuth, corrected of the bias computed in table 6. Average sun position is marked by an orange star. (negative values are in red and mean that MASTER is warmer than Landsat-8)

356 Figure 7 allows better observing those two configurations. It shows the distribu-
 357 tions of the bias-corrected SBT with respect to MASTER signed VZA (positive angle
 358 are to the east and therefore closer to the sun, negative to the west). The dotted red line
 359 indicates the mean difference, while the dashed red lines indicate ± 1 standard devia-
 360 tion. In configurations (2), (8) and (12) where the sun is almost in the principal plane
 361 and close to hotspot, MASTER SBT gets steadily warmer than Landsat-8 from east to
 362 west. For track (8), SBT starts to get colder past the sun zenith. For tracks (1), (3),
 363 (5), (6), (7) and (11), MASTER gets colder on both end of the swath, with a varying

364 position for the maximum position, which may be related to gap fraction. Dotted blue
 365 vertical lines indicate the FOV of the up-comping TRISHNA and SBG missions. One
 366 can note that the 1 standard deviation red dashed lines show that the standard deviation
 367 is almost constant throughout the MASTER signed VZA, and equal to standard
 368 deviation estimated in table 6. This standard deviation therefore probably accounts for
 369 uncertainties between sensors that are not related to TIR anisotropy.

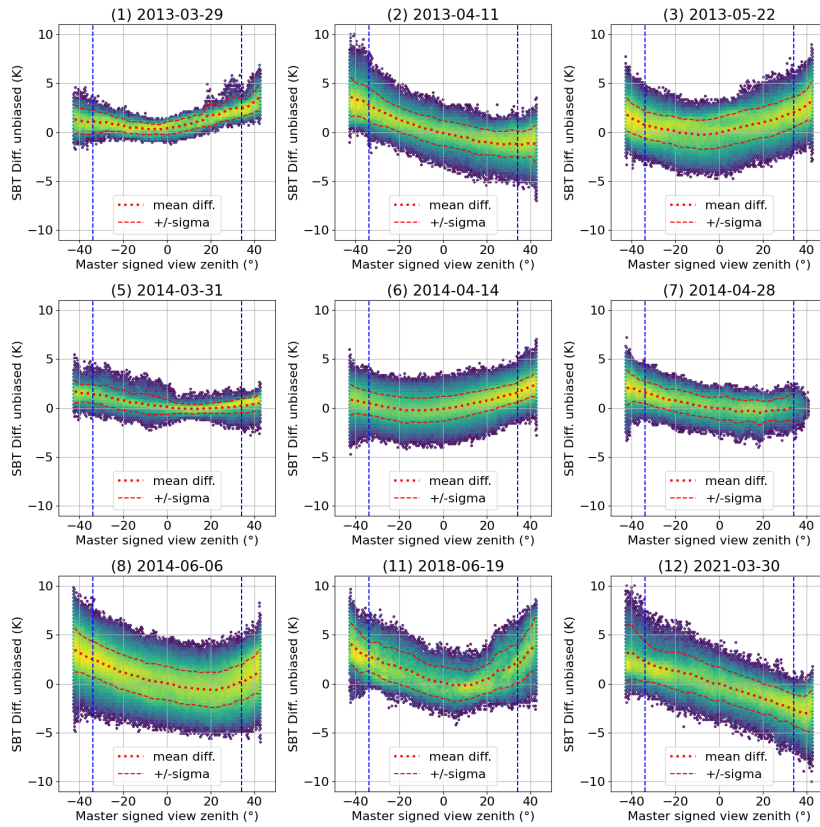


Figure 7: SBT difference, corrected of the bias computed in table 6, with respect to MASTER signed view zenith angle (positive angles are to the east, negative to the west). The solid red line indicates the mean values, the red dashed line indicates mean \pm 1 standard deviation. Blue dotted lines indicate TRISHNA and SBG FOV.

370 Table 7 gives a quantitative analysis of the directional effects budget for each track,
 371 based on the mean difference trend for each track (see dotted red curves in figure 7).

372 Within MASTER FOV, the amplitude of directional effects ranges from 1.5K to more
 373 than 6K for track (12), the closest track to hotspot conditions. Restricted to the foreseen
 374 TRISHNA and SBG FOV, this budget value falls to 4.7K.

id	MASTER				Trishna			
	Min.	-43°	43°	amp.	Min.	-34°	34°	amp.
(1) 2013-03-29	0.3	1.3	3.6	3.3	0.3	1.1	2.5	2.2
(2) 2013-04-11	-1.3	3.6	-1.2	4.9	-1.2	2.6	-1.2	3.9
(3) 2013-05-22	-0.3	1.8	3.2	3.4	-0.3	0.7	1.9	2.2
(5) 2014-03-31	-0.1	1.7	0.5	1.8	-0.1	1.4	0.2	1.5
(6) 2014-04-14	-0.3	0.8	2.4	2.7	-0.3	0.4	1.5	1.7
(7) 2014-04-28	-0.5	2.0	0.1	2.5	-0.5	1.5	-0.0	2.0
(8) 2014-06-06	-0.7	3.5	1.2	4.1	-0.7	2.5	0.1	3.1
(11) 2018-06-19	-0.2	4.1	4.0	4.3	-0.2	2.7	2.0	2.9
(12) 2021-03-30	-3.0	3.1	-2.9	6.3	-2.4	2.2	-2.5	4.7

Table 7: For each MASTER track, minimum average SBT difference, average SBT difference at both ends of swath and amplitude (amp.) of SBT difference between minimum and maximum are displayed, left for the MASTER FOV, right, for a limitation to TRISHNA FOV (all in K). The max-min column gives an estimate of directional effects.

375 3.2.3. Sensitivity to land-cover

376 Figure 8 shows the mean and standard deviation curves of SBT difference with re-
 377 spect to MASTER signed view zenith angle, for the major land-cover classes (> 15%)
 378 highlighted in table 5. It can be observed that though slight differences may appear
 379 between classes on the same track, most of the time all classes follow a similar trend
 380 for a given track. The NDVI strata seems to be the main driver for consistency, as can
 381 be noted on track (1) and (5) with bare soil and low vegetation with low NDVI, on
 382 track (3) with forests and low vegetation, both with intermediate NDVI, and on track
 383 (8) between croplands and low vegetation, both with a low NDVI. On track (6), it can
 384 be observed that the urban class behaves very similarly to the low vegetation with low
 385 NDVI class, which may indicate that urban class is actually a fair mix of artificial and

386 vegetated surfaces. Track (3) might exhibit some sort of gap fraction effect, with in-
387 termediate NDVI classes getting to a lower minimum than low NDVI classes. Forests
388 with high NDVI seem to behave slightly differently than other intermediate NDVI veg-
389 etation classes, with only two examples on track (7) and (12). Interestingly, forests
390 with high NDVI also exhibit a smaller standard deviation with respect to other classes.
391 Some kind of ordering can be observed for instance on track (7) and (11), with lower
392 NDVI classes yielding lower differences.

393 It should however be noted that in most of the cases, mean curves of each classes are
394 within the \pm standard-deviation of other classes. This seems to indicate that in the 100
395 meter resolution range, with this combination of limited dataset and land-cover source,
396 pixels are mixed and exhibit average directional trends rather than sharp vegetation
397 or crop types related signatures. Due to the severe classes imbalance between tracks,
398 estimating model parameters independently on each class would further reduce the
399 variability of angular configurations and thus the significance of the experiment. A
400 much larger dataset would be necessary for per-class estimation of models parameters.
401 In the next section, model estimations will therefore only be performed jointly for all
402 classes.

403 *3.3. Directional model fitting*

404 *3.3.1. Per-track parameters estimation*

405 In this section, each of the five models presented in table 3 is fitted independently
406 on de-biased SBT from each track, using the methodology presented in 2.3. Models are
407 fitted using all pixels from all land-cover classes of a track, which provides the required
408 variability to fit the 3 to 4 parameters depending on the model. Figure 9 shows how
409 each model fits the scatter plot for each track. SBT differences are expressed as a
410 percentage variation to facilitate the comparison with the model. All models seem to
411 be able to fit the observed directional effects, with the RL and LSF-RL being slightly
412 more versatile than the other, and the Vinnikov model struggling to cope with higher
413 VZA. This can be observed for instance on tracks (2) and (12) where the Vinnikov
414 model diverges below 0° . Hotspot shape seems to be correctly captured by the other
415 four models in track (2), (8) and (12). Differences for all models start to show for

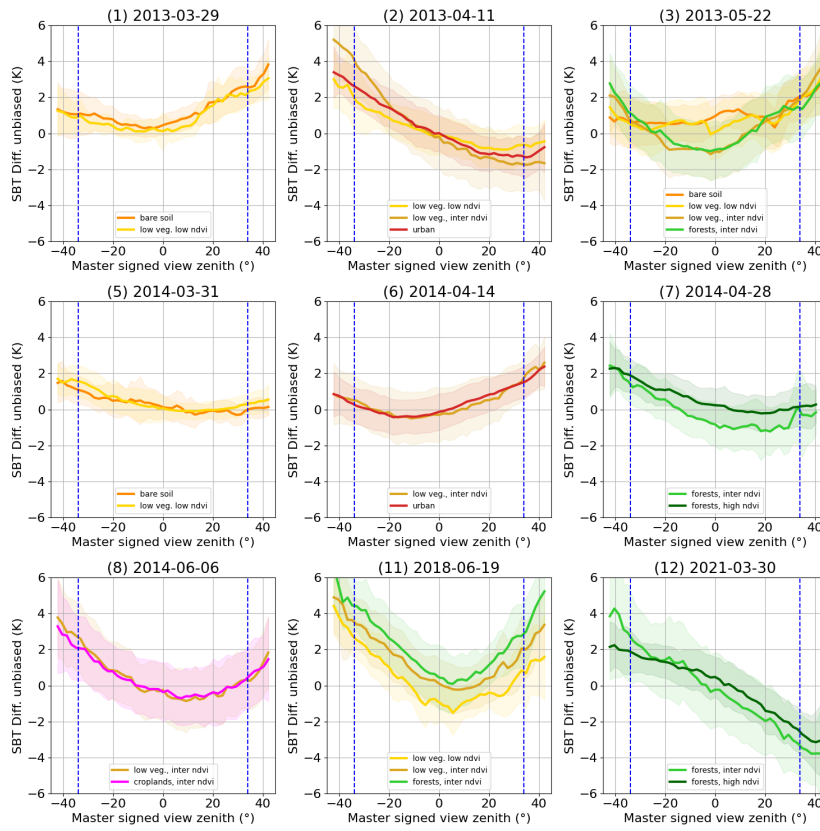


Figure 8: Mean \pm standard-deviation of unbiased SBT difference with respect to MASTER signed view zenith angle for the major land-cover classes (> 15%) of each land cover classes as highlighted in table 5.

416 higher viewing angles close to or outside limits of the data range.

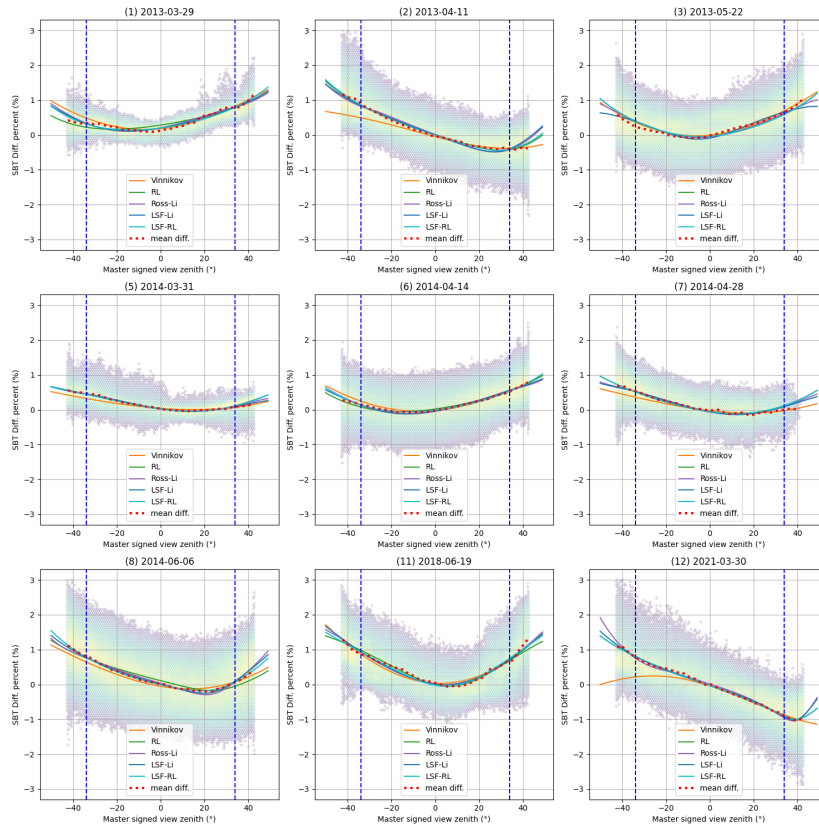


Figure 9: Least-Square fitting of the five TIR directional models from table 3 on SBT differences. Vertical axis represent the percentage of variation of SBT between Landsat-8 (considered as Nadir) and MASTER. In this figure, each model is fitted separately on each track.

417 In table 8, the correction performance of each model is measured for each track in
 418 terms of Root Mean Squared Error (RMSE) and amplitude (max - min of red curve
 419 in figure 7). Regarding RMSE, it can be observed that all models allow reducing the
 420 RMSE with respect to the uncorrected values. Though performances on RMSE im-
 421 provement are very close from one model to another, the LSF-Li reaches the best per-
 422 formances for 8 tracks out of 9, while the Ross-Li and LSF-RL models reaches the best
 423 performances on 7 tracks out of 9. On track (12), which is the closest to the hotspot,
 424 all models seem to perform almost equally. Gains on RMSE range from 0.2K to 0.9K

425 depending on the track.

426 In [Cao et al. \(2019\)](#), lower RMSE are found on simulated data (bellow 0.5K). Thea
 427 authors recommend the following ranking for models (best to worst) : LSF-Li, Ross-
 428 Li, Vinnikov and RL. This is consistent with RMSE on table 8 with the LSF-Li being
 429 the best model 8 times out of 9, the Ross-Li, Vinnikov and LSF-RL models 7 times out
 430 of 9, and the RL model only 5 times out of 9.

431 In terms of directional effects amplitude, table 8 shows that all models allow to
 432 significantly reduce the amplitude, below 1 K for the majority of tracks. Reductions
 433 for tracks with high hotspot effects are particularly strong, with track (12) going from
 434 more than 6K to less than 0.7 K for instance. The Vinnikov model is the best model
 435 for more than half of the tracks, but tracks with strong hotspot effect such as (8) and
 436 (12) are won by either RL, LSF-Li or LSF-RL. Regarding amplitude, performances
 437 of the different models are less close to each others, but this can be explained by the
 438 use of maximum - minimum difference, which is highly sensitive to outliers. Gains on
 439 directional effects amplitude range from 1.6K to 5.8K depending on the track.

id	RMSE						Amp					
	Raw	Vin.	RL	Ross	LSF	LRL	Raw	Vin.	RL	Ross	LSF	LRL
(1)	1.8	1.0	1.0	1.0	1.0	1.0	3.3	0.6	1.4	1.0	0.8	0.9
(2)	2.3	1.5	1.5	1.5	1.5	1.5	4.9	0.3	0.6	1.1	1.1	0.7
(3)	2.0	1.5	1.6	1.6	1.5	1.6	3.4	0.5	1.2	1.0	1.2	0.9
(5)	1.1	0.8	0.8	0.8	0.8	0.8	1.8	0.4	0.4	0.3	0.2	0.4
(6)	1.6	1.2	1.2	1.2	1.2	1.2	2.7	0.2	0.4	0.6	0.5	0.3
(7)	1.6	1.2	1.2	1.2	1.2	1.2	2.5	0.3	0.9	0.8	0.8	0.9
(8)	2.3	1.8	1.9	1.8	1.8	1.8	4.1	0.8	1.3	0.7	0.4	0.2
(11)	2.8	1.9	1.9	1.9	1.9	1.8	4.3	1.1	1.4	0.9	1.0	1.0
(12)	2.7	1.9	1.9	1.8	1.8	1.9	6.3	0.7	0.5	0.7	0.5	0.5

Table 8: Root Mean-Square error and amplitude (max - min of red curve in figure 7) for raw SBT corrected of the bias computed in table 6, and for MASTER temperature normalized with five models, with parameters estimated for each track. Note that model names have been shortened (Vin: Vinnikov, RL: Roujean-Lagouarde, Ross: Ross-Li, LSF: LSF-Li, LRL: LSF-RL).

440 Figure 10 shows the raw and corrected SBT with respect to the signed VZA for 5
441 tracks with very strong directional effects. It can be noted that the correction does not
442 seem to have any effect on the standard-deviation, and thus it does not amplify or create
443 any noise. For track (2), the best model in terms of amplitude is Vinnikov according
444 to table 8, closely followed by RL and LSF, though it can be observed that the Ross-Li
445 and LSF-Li models struggle at higher VZA (out of TRISHNA FOV). For track (3), the
446 best model is also Vinnikov, with amplitude two times less than the next best model,
447 which is RL. Indeed, the latter seems to fail to completely compensate the directional
448 trends, with SBT differences still slightly positives for positive VZA and negative for
449 negative VZA. On track (8), the best model is LSF-RL by a large amount according to
450 table 8, which is confirmed on figure 10 with a smooth a regular corrected SBT.

451 Although directional trends are considerably reduced after correction, there are re-
452 maining trends in almost all models, and all of them struggle at higher VZA. Track (11)
453 is noisier and the model fitting is poorer, with only the Ross-Li model achieving a cor-
454 rection with an amplitude below 1 K, though differences on figure 10 are not obvious.
455 For track (12), which is the track with the strongest hotspot effect due to the proxim-
456 ity of MASTER viewing direction and solar direction (see figure 6), LSF-Li, RL and
457 LSF-RL models have the best performances according to table 8 which is confirmed
458 on figure 10 by fewer oscillations for higher VZA.

459 3.3.2. *Global models parameters estimation*

460 Fitting models on each track separately allows to assess how well those models ex-
461 plain the observed data. However, this strategy does not apply to operational directional
462 corrections in ground segments, where simultaneous observations will not be available
463 to fit the models. This section investigates the performances of global models, with
464 a single set of parameters for each model to correct all tracks at once. Parameters of
465 those global models are fitted on all pixels from all tracks altogether, using the method-
466 ology presented in 2.3. Figure 11 shows how well those global models fit the scatter
467 plots for each track. It can be observed that even if the goodness of fit is lesser than in
468 figure 9, it is still relatively high. However, global models also struggle to model the
469 near hotspot conditions of track (12).

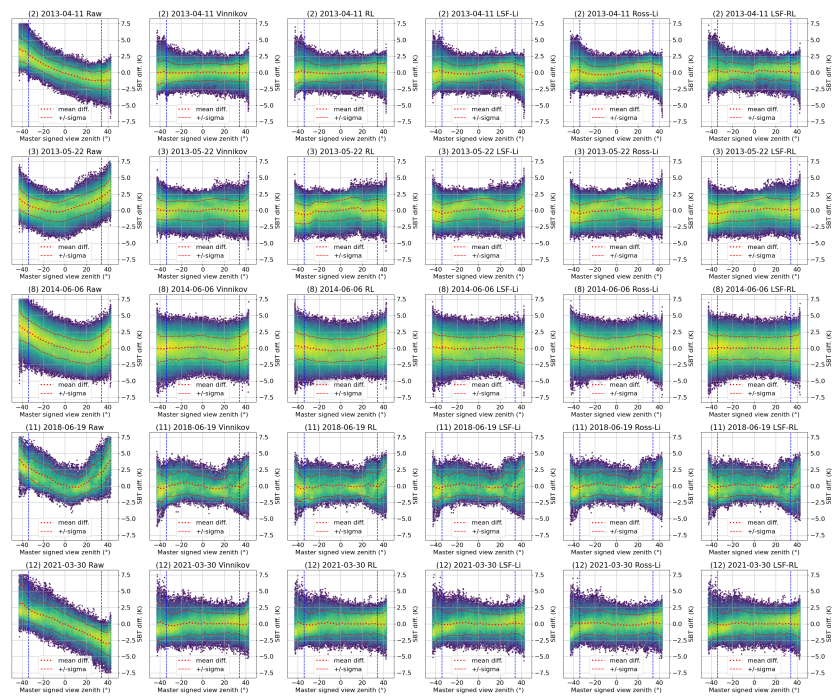


Figure 10: Corrected SBT versus signed VZA for raw and model-corrected SBT, for 5 tracks with high directional effects amplitudes. Blue dashed lines indicate Trishna FOV.

470 Table 9 shows the quantitative performance analysis of global models. As in table
471 8, no model clearly outperform the others. All models achieve a systematic decrease
472 of RMSE ranging from 0.2K to 0.9K and a systematic decrease of directional effects
473 amplitude ranging from 1.3K to 4.8K. Even if their performances are lower than those
474 achieved by per track models presented in section 3.3.1, global models still provide
475 valuable corrections. It can be observed that if the RL model is frequently the best
476 model in terms of RMSE, it is never the best model in terms of amplitude. The ranking
477 according to the number of times a model is the best model in terms of RMSE is the
478 following (best to worst) : RL, LSF-RL, Vinnikov and LSF-Li, Ross-Li. This ranking
479 differs from the ranking of Cao et al. (2019), in which models are not fitted globally.

id	RMSE						Amp					
	Raw	Vin.	RL	Ross	LSF	LRL	Raw	Vin.	RL	Ross	LSF	LRL
(1)	1.8	1.2	1.3	1.0	1.0	1.2	3.3	1.2	1.2	1.6	0.9	1.0
(2)	2.3	1.5	1.6	1.6	1.6	1.6	4.9	1.0	1.8	1.8	2.2	2.0
(3)	2.0	1.6	1.6	1.6	1.6	1.6	3.4	1.2	1.3	1.4	1.2	1.4
(5)	1.1	0.9	0.8	1.2	1.1	0.8	1.8	1.1	0.6	0.5	1.1	0.7
(6)	1.6	1.2	1.2	1.2	1.2	1.2	2.7	0.6	0.5	0.7	0.7	0.3
(7)	1.6	1.2	1.2	1.3	1.3	1.2	2.5	0.8	0.9	1.0	1.4	1.0
(8)	2.3	1.9	1.9	2.0	1.9	1.9	4.1	1.4	1.9	1.9	1.0	1.4
(11)	2.8	2.2	1.9	2.2	2.1	1.9	4.3	2.8	2.1	2.8	1.9	1.9
(12)	2.7	2.1	2.0	2.1	2.0	2.1	6.3	2.5	2.7	1.7	1.5	3.2

Table 9: Root Mean-Square error and amplitude (max - min of red curve in figure 7) for raw SBT corrected of the bias computed in table 6, and for MASTER temperature normalized with five models, with parameters jointly estimated on all tracks. Note that model names have been shortened (Vin: Vinnikov, RL: Roujean-Lagouarde, Ross: Ross-Li, LSF: LSF-Li, LRL: LSF-RL).

480 Figure 12 presents the same tracks as in figure 10 but corrected with the global
481 models. While all tracks exhibit residual angular trends, within the TRISHNA FOV,
482 all models exhibit performances that may be of interest for downstream applications.
483 Track (11) has the highest residual effects, which is compliant with figures in table 9,

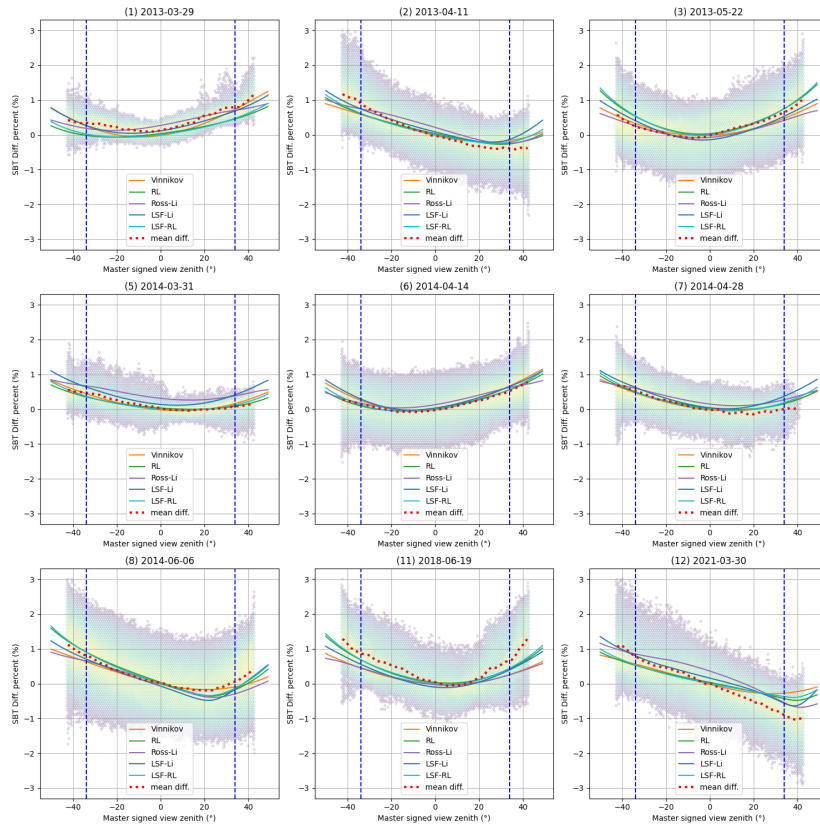


Figure 11: Least-Square fitting of the five TIR directional models from table 3 on SBT differences. Vertical axis represent the percentage of variation of SBT between Landsat-8 (considered as Nadir) and MASTER. In this figure, each model is jointly fitted on all tracks.

484 showing a residual amplitude of around 2K for all models. On track (12), which is the
 485 closest to hotspot conditions, the Vinnikov and LSF-RL model perform poorly with
 486 respect to the other models, the former even introduces an artificial angular trend while
 487 the latter fails to completely capture the angular tend. All remaining models on track
 488 (12) significantly reduce the angular trend that can be observed in raw SBT differences.

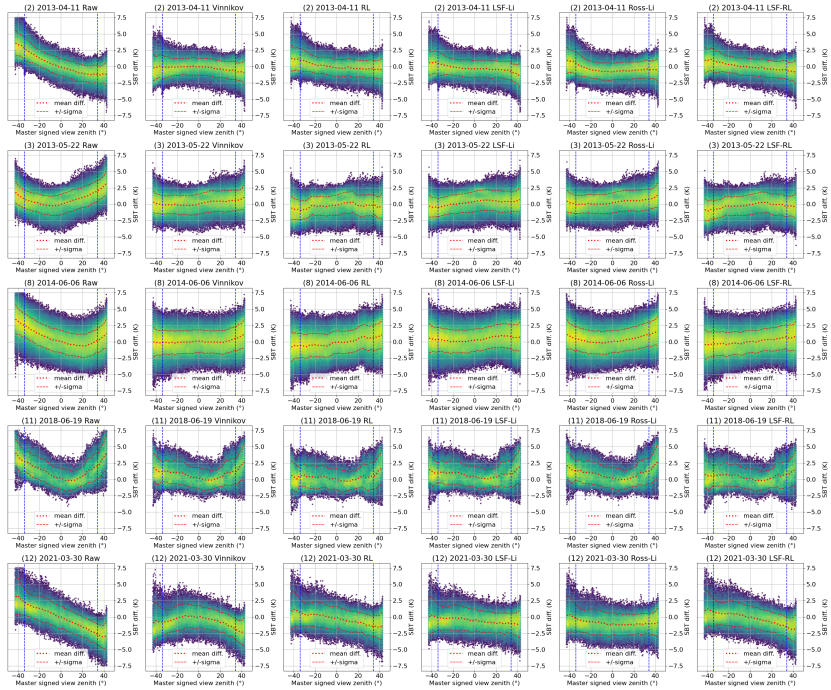


Figure 12: Corrected SBT versus signed VZA for raw and model-corrected SBT, using models jointly fitted on all tracks, for 5 tracks with high directional effects amplitudes. Blue dashed lines indicate TRISHNAP FOV.

489 Figure 13 presents a complete viewing angles sampling of each global model, in
 490 the mean solar conditions of track (12). All models seem to have captured the hotspot
 491 effect, while the shape of the hotspot itself varies from one model to another. the
 492 Vinnikov model hotspot seems ahead of the sun zenith angle, which may explain its
 493 lesser performance in correcting track (12). Table 10 shows the estimated parameters
 494 for each model. One can note that the Ross-Li Volumetric kernel contribution is very
 495 low with respect to the others.

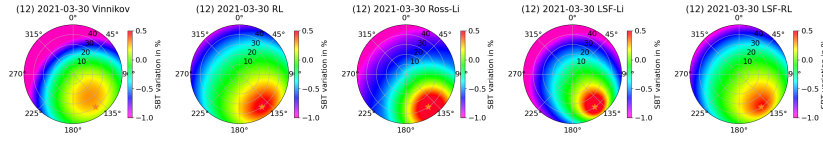


Figure 13: Polar plot of the different models, jointly fitted on all tracks, using average solar angles of track (12). Sun position is indicated by an orange star mark.

Model	k_0	k_1	k_2	k_{hs}
Ross-Li	1	-7.4e-16	0.0091	
LSF-Li	1.2	-0.22	0.011	
Vinnikov	1	-0.023	0.024	
RL	1		0.0061	1.8e-07
LSF-RL	1	-0.047	0.0058	9.7e-07

Table 10: Parameters of the global models, estimated from all pairs

496 4. Discussion

497 This study exhibits evidences of strong directional effects up to an amplitude of
 498 6K within a FOV of $\pm 45^\circ$, with real high-resolution TIR data, and shows encouraging
 499 performances of state-of-the art parametric models to mitigate their impact on temper-
 500 ature accuracy. However, two aspects of this work need to be further analysed and
 501 discussed: the inherent limitations related to the scarce data availability on one hand,
 502 and the derivation of the model parameters in a real-world ground segment scenario.

503 4.1. Limitations of the study

504 Due to the scarce availability of simultaneous observations between MASTER and
 505 Landsat-8 on one hand, and the limited coverage of MASTER flights on the other, this
 506 study only covers a limited range of landscapes, all of them located in California, USA.
 507 Therefore, it can not be used to draw solid conclusions on other kinds of landscapes
 508 such as desert bare soil, very dense rain-forest canopy or tundras for instance. The ge-
 509 ographic limitations also come with a low variety of solar angle conditions, excluding
 510 extreme latitudes and equator for instance.

511 Moreover, since this study relies on Landsat-8 acquisitions which have a local over-
512 passing time of approximately 10:30 AM, its results are mainly valid for medium morn-
513 ing sun angles, whereas most upcoming missions will have a local over-passing time
514 around noon. The solar zenith angle will therefore be lower, leading to solar angular
515 conditions that have not been analysed in this study. As hotspot conditions will be
516 more frequent, It is conjectured to observe lower but more frequent directional effects
517 for sun position closer to zenith, but in the mean time SBT values could be higher.

518 Finally, this study adopts an indiscriminating point of view regarding the actual
519 land-cover of each pixel, whereas the literature, which is driven by work on radiative
520 transfer modeling, strongly suggests that different models or at least model parameters
521 should be applied to different land-covers. We analysed the influence of land-cover on
522 TIR anisotropy in section 3.2.3. We observed that classes seem to be mixed in our 100
523 meter resolution dataset, and exhibit similar angular trends. The land-cover agnostic
524 approach was therefore privileged. However, this could be revisited if a larger dataset
525 was to be acquired, with more landscape variability. It must be stressed that if a direc-
526 tional effect correction is to be implemented into up-coming missions ground-segment
527 as a routine level 2 processing, relying on land-cover discrimination and phenology
528 will be hard to achieve for a global coverage mission. Nevertheless, exogenous land-
529 cover and phenology maps could be used for that purpose (Phiri et al., 2020). Last,
530 TIR directional effects in urban environment follow very different physical causes and
531 trends (Lagouarde and Irvine, 2008; Lagouarde et al., 2010), and may require different
532 models, such as the combinations of base kernels investigated in Jiang et al. (2021).

533 *4.2. Model parameters estimation for up-coming ground segments*

534 Another open question is whether such a correction is to be implemented within
535 future ground segments and which credit to give to the estimated model parameters
536 over time. In this study, models have first been fitted to each track independently, re-
537 sulting in good correction performances of up to 5.8K in amplitude, but with important
538 variations of the parameters from one track to another. Such variability suggests that
539 model parameters might depend on the canopy structure as well as on the observation
540 conditions they are fitted to. For instance, the RL kernel, is the best performing kernel

541 for track (12) that is closest to hotspot condition, which can be explained either because
542 this model is a good model for hotspot or because it requires hotspot condition to be
543 fitted properly. It must however again be stressed that such scene based individual pa-
544 rameters estimation is out of reach for routinely correcting data from global coverage
545 satellites such as TRISHNA, LSTM or SBG.

546 On the other hand, the global models that have been fitted simultaneously on all
547 tracks still exhibit interesting correction performances of up to 4.7K in the studied
548 tracks. This work therefore suggests that such global models could be used routinely
549 in a ground segment and be beneficial for downstream applications, with the limitations
550 already highlighted in section 4.1.

551 While the determination of factors that should drive model parameters is probably
552 best served by the physical process modelling scientific community, this paper pro-
553 poses valuable dataset and methodology to assess model performances before putting
554 them into production. Though in this work the analysed data are limited to 9 tracks
555 in California, in the future, MASTER or other airborne TIR sensors with wide FOVs
556 might be used to acquire more of those simultaneous observations with the Landsat
557 series, effectively building a database for the assessment and calibration of directional
558 parametric models, should attention be paid to the simultaneous over-passing time.

559 **5. Conclusion**

560 In this paper, simultaneous observations in space and time between Landsat-8 and
561 the wide FOV MASTER airborne TIR sensors have been leveraged to analyse potential
562 directional effects and their error budget for up-coming High Resolution TIR missions.
563 Nine MASTER tracks were identified with a Landsat-8 overpass during the flight and
564 the analysis of their SBT differences exhibits directional effects ranging from 1.6K to
565 more than 6K within MASTER full FOV depending to the proximity to hotspot con-
566 ditions. Three tracks are close to those conditions and one is almost within the prin-
567 cipal acquisition plane, leading to the highest 6K amplitude. Other tracks also exhibit
568 evidences of the gap fraction effect. Five state-of-the-art parametric models for TIR
569 anisotropy have been selected from the literature for having been extensively tested on

570 simulated data. Those five models have been fitted to each of the identified MASTER
571 track, using Landsat-8 as the target Nadir SBT of reference. The corrected temperature
572 exhibits a systematic decrease of the RMSE of 0.2K to 0.9K, and a reduction of the am-
573 plitude associated to directional effects of 1.6K to 5.8K, bringing down the directional
574 error budget to less than 1K in almost all cases. Global models, fitted simultaneously
575 on all valid tracks, have also been assessed, with a reduction of RMSE of 0.2K to 0.8K
576 and a reduction of the directional effect amplitude of 1.3K to 4.7K, bringing down
577 the directional error budget below 2K in most cases. Those results suggest that future
578 ground segments of up-coming high-resolution missions with a FOV greater than 30°
579 would benefit from implementing such a correction. This paper also lays grounds for a
580 directional model in flight calibration procedure for those up-coming missions, should
581 more airborne data be gathered during Landsat overpasses in the future.

582 The data used in this study have been made publicly available as an open dataset (Michel
583 et al., 2023).

584 **References**

585 M. Anderson, J. Norman, W. Kustas, R. Houborg, P. Starks, N. Agam, A
586 thermal-based remote sensing technique for routine mapping of land-surface car-
587 bon, water and energy fluxes from field to regional scales, *Remote Sensing*
588 of Environment 112 (2008) 4227–4241. URL: <https://www.sciencedirect.com/science/article/pii/S0034425708002289>. doi:<https://doi.org/10.1016/j.rse.2008.07.009>.

591 J. C. Price, Estimation of Regional Scale Evapotranspiration Through Analysis of
592 Satellite Thermal-infrared Data, *IEEE Transactions on Geoscience and Remote*
593 *Sensing GE-20* (1982) 286–292. doi:[10.1109/TGRS.1982.350445](https://doi.org/10.1109/TGRS.1982.350445), conference
594 Name: *IEEE Transactions on Geoscience and Remote Sensing*.

595 D. Courault, B. Seguin, A. Olioso, Review on estimation of evapotranspiration from
596 remote sensing data: From empirical to numerical modeling approaches, *Irrigation*
597 *and Drainage Systems* 19 (2005) 223–249. URL: <https://doi.org/10.1007/s10795-005-5186-0>. doi:[10.1007/s10795-005-5186-0](https://doi.org/10.1007/s10795-005-5186-0).

- 599 M. C. Anderson, R. G. Allen, A. Morse, W. P. Kustas, Use of Landsat thermal im-
600 agery in monitoring evapotranspiration and managing water resources, *Remote*
601 *Sensing of Environment* 122 (2012) 50–65. URL: [https://www.sciencedirect.](https://www.sciencedirect.com/science/article/pii/S0034425712000326)
602 [com/science/article/pii/S0034425712000326](https://www.sciencedirect.com/science/article/pii/S0034425712000326). doi:10.1016/j.rse.2011.
603 08.025.
- 604 G. Boulet, B. Mougenot, J.-P. Lhomme, P. Fanise, Z. Lili-Chabaane, A. Olioso,
605 M. Bahir, V. Rivalland, L. Jarlan, O. Merlin, B. Coudert, S. Er-Raki, J.-
606 P. Lagouarde, The SPARSE model for the prediction of water stress and
607 evapotranspiration components from thermal infra-red data and its evaluation
608 over irrigated and rainfed wheat, *Hydrology and Earth System Sciences*
609 19 (2015) 4653–4672. URL: [https://hess.copernicus.org/articles/19/](https://hess.copernicus.org/articles/19/4653/2015/)
610 [4653/2015/](https://hess.copernicus.org/articles/19/4653/2015/). doi:10.5194/hess-19-4653-2015, publisher: Copernicus GmbH.
- 611 R. Ishimwe, K. Abutaleb, F. Ahmed, et al., Applications of thermal imaging in agri-
612 culture—a review, *Advances in remote Sensing* 3 (2014) 128.
- 613 J.-P. Lagouarde, B. Bhattacharya, P. Crébassol, P. Gamet, S. S. Babu, G. Boulet,
614 X. Briottet, K. Buddhiraju, S. Cherchali, I. Dadou, G. Dedieu, M. Gouhier,
615 O. Hagolle, M. Irvine, F. Jacob, A. Kumar, K. K. Kumar, B. Laignel, K. Mallick,
616 C. Murthy, A. Olioso, C. Ottlé, M. R. Pandya, P. V. Raju, J.-L. Roujean, M. Sekhar,
617 M. V. Shukla, S. K. Singh, J. Sobrino, R. Ramakrishnan, The Indian-French Trishna
618 Mission: Earth Observation in the Thermal Infrared with High Spatio-Temporal
619 Resolution, in: *IGARSS 2018 - 2018 IEEE International Geoscience and Remote*
620 *Sensing Symposium, 2018*, pp. 4078–4081. doi:10.1109/IGARSS.2018.8518720,
621 iSSN: 2153-7003.
- 622 K. Cawse-Nicholson, P. A. Townsend, D. Schimel, A. M. Assiri, P. L. Blake, M. F.
623 Buongiorno, P. Campbell, N. Carmon, K. A. Casey, R. E. Correa-Pabón, K. M.
624 Dahlin, H. Dashti, P. E. Dennison, H. Dierssen, A. Erickson, J. B. Fisher, R. Frouin,
625 C. K. Gatebe, H. Gholizadeh, M. Gierach, N. F. Glenn, J. A. Goodman, D. M. Grif-
626 fith, L. Guild, C. R. Hakkenberg, E. J. Hochberg, T. R. H. Holmes, C. Hu, G. Hul-
627 ley, K. F. Huemmrich, R. M. Kudela, R. F. Kokaly, C. M. Lee, R. Martin, C. E.

- 628 Miller, W. J. Moses, F. E. Muller-Karger, J. D. Ortiz, D. B. Otis, N. Pahlevan, T. H.
629 Painter, R. Pavlick, B. Poulter, Y. Qi, V. J. Realmuto, D. Roberts, M. E. Schaepman,
630 F. D. Schneider, F. M. Schwandner, S. P. Serbin, A. N. Shiklomanov, E. N. Stavros,
631 D. R. Thompson, J. L. Torres-Perez, K. R. Turpie, M. Tzortziou, S. Ustin, Q. Yu,
632 Y. Yusup, Q. Zhang, NASA's surface biology and geology designated observable:
633 A perspective on surface imaging algorithms, *Remote Sensing of Environment* 257
634 (2021) 112349. URL: [https://www.sciencedirect.com/science/article/
635 pii/S0034425721000675](https://www.sciencedirect.com/science/article/pii/S0034425721000675). doi:10.1016/j.rse.2021.112349.
- 636 B. Koetz, W. Bastiaanssen, M. Berger, P. Defournay, U. Del Bello, M. Drusch,
637 M. Drinkwater, R. Duca, V. Fernandez, D. Ghent, R. Guzinski, J. Hoozeveld,
638 S. Hook, J.-P. Lagouarde, G. Lemoine, I. Manolis, P. Martimort, J. Masek, M. Mas-
639 sart, C. Notarnicola, J. Sobrino, T. Udelhoven, High Spatio- Temporal Resolution
640 Land Surface Temperature Mission - a Copernicus Candidate Mission in Support of
641 Agricultural Monitoring, in: *IGARSS 2018 - 2018 IEEE International Geoscience
642 and Remote Sensing Symposium*, 2018, pp. 8160–8162. doi:10.1109/IGARSS.
643 2018.8517433, iSSN: 2153-7003.
- 644 S. Mwangi, G. Boulet, A. Olioso, Assessment of an extended sparse model for esti-
645 mating evapotranspiration from directional thermal infrared data, *Agricultural and
646 Forest Meteorology* 317 (2022) 108882. URL: [http://dx.doi.org/10.1016/j.
647 agrformet.2022.108882](http://dx.doi.org/10.1016/j.agrformet.2022.108882). doi:10.1016/j.agrformet.2022.108882.
- 648 Z.-L. Li, B.-H. Tang, H. Wu, H. Ren, G. Yan, Z. Wan, I. F. Trigo, J. A. Sobrino,
649 Satellite-derived land surface temperature: Current status and perspectives, *Remote
650 Sensing of Environment* 131 (2013) 14–37. URL: [http://dx.doi.org/10.1016/
651 j.rse.2012.12.008](http://dx.doi.org/10.1016/j.rse.2012.12.008). doi:10.1016/j.rse.2012.12.008.
- 652 D. L. Jupp, A. H. Strahler, A hotspot model for leaf canopies, *Remote Sensing of
653 Environment* 38 (1991) 193–210.
- 654 T. Nilson, Inversion of gap frequency data in forest stands, *Agricultural and For-
655 est Meteorology* 98-99 (1999) 437–448. URL: [http://dx.doi.org/10.1016/
656 S0168-1923\(99\)00114-8](http://dx.doi.org/10.1016/S0168-1923(99)00114-8). doi:10.1016/s0168-1923(99)00114-8.

- 657 J.-P. Lagouarde, S. Dayau, P. Moreau, D. Guyon, Directional anisotropy of brightness
658 surface temperature over vineyards: Case study over the medoc region (sw france),
659 IEEE Geoscience and Remote Sensing Letters 11 (2014) 574–578. doi:10.1109/
660 LGRS.2013.2282492.
- 661 J. A. Sobrino, J. Cuenca, Angular variation of thermal infrared emissivity for some
662 natural surfaces from experimental measurements, Applied Optics 38 (1999)
663 3931. URL: <http://dx.doi.org/10.1364/ao.38.003931>. doi:10.1364/ao.
664 38.003931.
- 665 S. L. Ermida, I. F. Trigo, G. Hulley, C. C. DaCamara, A multi-sensor approach to re-
666 trieve emissivity angular dependence over desert regions, Remote Sensing of Envi-
667 ronment 237 (2020) 111559. URL: [http://dx.doi.org/10.1016/j.rse.2019.](http://dx.doi.org/10.1016/j.rse.2019.111559)
668 [111559](http://dx.doi.org/10.1016/j.rse.2019.111559). doi:10.1016/j.rse.2019.111559.
- 669 J.-L. Roujean, M. Leroy, P.-Y. Deschamps, A bidirectional reflectance model of the
670 earth's surface for the correction of remote sensing data, Journal of Geophys-
671 ical Research 97 (1992) 20455. URL: <http://dx.doi.org/10.1029/92jd01411>.
672 doi:10.1029/92jd01411.
- 673 W. Wanner, X. Li, A. H. Strahler, On the derivation of kernels for kernel-driven models
674 of bidirectional reflectance, Journal of Geophysical Research 100 (1995) 21077.
675 URL: <http://dx.doi.org/10.1029/95jd02371>. doi:10.1029/95jd02371.
- 676 J.-L. Roujean, A parametric hot spot model for optical remote sensing applications,
677 Remote Sensing of Environment 71 (2000) 197–206. URL: [http://dx.doi.org/](http://dx.doi.org/10.1016/s0034-4257(99)00080-2)
678 [10.1016/s0034-4257\(99\)00080-2](http://dx.doi.org/10.1016/s0034-4257(99)00080-2). doi:10.1016/s0034-4257(99)00080-2.
- 679 M. Claverie, J. Ju, J. G. Masek, J. L. Dungan, E. F. Vermote, J.-C. Roger, S. V.
680 Skakun, C. Justice, The harmonized landsat and sentinel-2 surface reflectance
681 data set, Remote Sensing of Environment 219 (2018) 145 – 161. doi:[https:](https://doi.org/10.1016/j.rse.2018.09.002)
682 [//doi.org/10.1016/j.rse.2018.09.002](https://doi.org/10.1016/j.rse.2018.09.002).
- 683 C. Duffour, J.-P. Lagouarde, A. Olioso, J. Demarty, J.-L. Roujean, Driving factors of

- 684 the directional variability of thermal infrared signal in temperate regions, *Remote*
685 *Sensing of Environment* 177 (2016) 248–264.
- 686 B. Cao, Q. Liu, Y. Du, J.-L. Roujean, J.-P. Gastellu-Etchegorry, I. F. Trigo, W. Zhan,
687 Y. Yu, J. Cheng, F. Jacob, et al., A review of earth surface thermal radiation direc-
688 tionality observing and modeling: Historical development, current status and per-
689 spectives, *Remote Sensing of Environment* 232 (2019) 111304.
- 690 Z. Bian, J.-L. Roujean, J.-P. Lagouarde, B. Cao, H. Li, Y. Du, Q. Liu, Q. Xiao, Q. Liu,
691 A semi-empirical approach for modeling the vegetation thermal infrared directional
692 anisotropy of canopies based on using vegetation indices, *ISPRS Journal of Pho-*
693 *togrammetry and Remote Sensing* 160 (2020) 136–148. URL: [http://dx.doi.](http://dx.doi.org/10.1016/j.isprsjprs.2019.12.004)
694 [org/10.1016/j.isprsjprs.2019.12.004](http://dx.doi.org/10.1016/j.isprsjprs.2019.12.004). doi:10.1016/j.isprsjprs.2019.
695 12.004.
- 696 Z. Bian, J. Roujean, T. Fan, Y. Dong, T. Hu, B. Cao, H. Li, Y. Du, Q. Xiao,
697 Q. Liu, An angular normalization method for temperature vegetation dryness in-
698 dex (tvdI) in monitoring agricultural drought, *Remote Sensing of Environment*
699 284 (2023) 113330. URL: <http://dx.doi.org/10.1016/j.rse.2022.113330>.
700 doi:10.1016/j.rse.2022.113330.
- 701 P. Yang, E. Prikaziuk, W. Verhoef, C. van der Tol, Scope 2.0: a model to simulate veg-
702 etated land surface fluxes and satellite signals, *Geoscientific Model Development* 14
703 (2021) 4697–4712. URL: <http://dx.doi.org/10.5194/gmd-14-4697-2021>.
704 doi:10.5194/gmd-14-4697-2021.
- 705 J. Gastellu-Etchegorry, Modeling radiative transfer in heterogeneous 3-d veg-
706 etation canopies, *Remote Sensing of Environment* 58 (1996) 131–156.
707 URL: [http://dx.doi.org/10.1016/0034-4257\(95\)00253-7](http://dx.doi.org/10.1016/0034-4257(95)00253-7). doi:10.1016/
708 0034-4257(95)00253-7.
- 709 J.-P. Gastellu-Etchegorry, N. Lauret, T. Yin, L. Landier, A. Kallel, Z. Malenovsky,
710 A. A. Bitar, J. Aval, S. Benhmida, J. Qi, G. Medjdoub, J. Guilleux, E. Chavanon,
711 B. Cook, D. Morton, N. Chrysoulakis, Z. Mitraka, Dart: Recent advances in remote

- 712 sensing data modeling with atmosphere, polarization, and chlorophyll fluorescence,
713 IEEE Journal of Selected Topics in Applied Earth Observations and Remote Sensing
714 10 (2017) 2640–2649. URL: [http://dx.doi.org/10.1109/jstars.2017.](http://dx.doi.org/10.1109/jstars.2017.2685528)
715 [2685528](http://dx.doi.org/10.1109/jstars.2017.2685528). doi:[10.1109/jstars.2017.2685528](https://doi.org/10.1109/jstars.2017.2685528).
- 716 S. L. Ermida, I. F. Trigo, C. C. DaCamara, J.-L. Roujean, Assessing
717 the potential of parametric models to correct directional effects on local to
718 global remotely sensed LST, Remote Sensing of Environment 209 (2018)
719 410–422. URL: [https://www.sciencedirect.com/science/article/pii/](https://www.sciencedirect.com/science/article/pii/S0034425718300798)
720 [S0034425718300798](https://www.sciencedirect.com/science/article/pii/S0034425718300798). doi:[10.1016/j.rse.2018.02.066](https://doi.org/10.1016/j.rse.2018.02.066).
- 721 B. Cao, J.-L. Roujean, J.-P. Gastellu-Etchegorry, Q. Liu, Y. Du, J.-P. Lagouarde,
722 H. Huang, H. Li, Z. Bian, T. Hu, B. Qin, X. Ran, Q. Xiao, A general framework
723 of kernel-driven modeling in the thermal infrared domain, Remote Sensing of Envi-
724 ronment 252 (2021) 112157. URL: [http://dx.doi.org/10.1016/j.rse.2020.](http://dx.doi.org/10.1016/j.rse.2020.112157)
725 [112157](http://dx.doi.org/10.1016/j.rse.2020.112157). doi:[10.1016/j.rse.2020.112157](https://doi.org/10.1016/j.rse.2020.112157).
- 726 A. Pinheiro, J. Privette, P. Guillevic, Modeling the observed angular anisotropy of
727 land surface temperature in a savanna, IEEE Transactions on Geoscience and Re-
728 mote Sensing 44 (2006) 1036–1047. URL: [http://dx.doi.org/10.1109/tgrs.](http://dx.doi.org/10.1109/tgrs.2005.863827)
729 [2005.863827](http://dx.doi.org/10.1109/tgrs.2005.863827). doi:[10.1109/tgrs.2005.863827](https://doi.org/10.1109/tgrs.2005.863827).
- 730 Z. Bian, B. Cao, H. Li, Y. Du, J.-P. Lagouarde, Q. Xiao, Q. Liu, An analytical four-
731 component directional brightness temperature model for crop and forest canopies,
732 Remote Sensing of Environment 209 (2018) 731–746. URL: [http://dx.doi.org/](http://dx.doi.org/10.1016/j.rse.2018.03.010)
733 [10.1016/j.rse.2018.03.010](http://dx.doi.org/10.1016/j.rse.2018.03.010). doi:[10.1016/j.rse.2018.03.010](https://doi.org/10.1016/j.rse.2018.03.010).
- 734 B. Cao, J.-P. Gastellu-Etchegorry, Y. Du, H. Li, Z. Bian, T. Hu, W. Fan, Q. Xiao, Q. Liu,
735 Evaluation of four kernel-driven models in the thermal infrared band, IEEE Transac-
736 tions on Geoscience and Remote Sensing 57 (2019) 5456–5475. URL: [http://dx.](http://dx.doi.org/10.1109/TGRS.2019.2899600)
737 [doi.org/10.1109/TGRS.2019.2899600](http://dx.doi.org/10.1109/TGRS.2019.2899600). doi:[10.1109/tgrs.2019.2899600](https://doi.org/10.1109/tgrs.2019.2899600).
- 738 C. Duffour, J. P. Lagouarde, J. L. Roujean, A two parameter model to simulate
739 thermal infrared directional effects for remote sensing applications, Remote Sens-
740 ing of Environment 186 (2016) 250–261. URL: [https://www.sciencedirect.](https://www.sciencedirect.com/science/article/pii/S0034425716300798)

741 com/science/article/pii/S0034425716303157. doi:10.1016/j.rse.2016.
742 08.012.

743 K. Y. Vinnikov, Y. Yu, M. D. Goldberg, D. Tarpley, P. Romanov, I. Laszlo, M. Chen,
744 Angular anisotropy of satellite observations of land surface temperature, *Geophys-*
745 *ical Research Letters* 39 (2012) n/a–n/a. URL: [http://dx.doi.org/10.1029/](http://dx.doi.org/10.1029/2012gl1054059)
746 [2012gl1054059](http://dx.doi.org/10.1029/2012gl1054059). doi:10.1029/2012gl1054059.

747 P. C. Guillevic, A. Bork-Unkelbach, F. M. Gottsche, G. Hulley, J.-P. Gastellu-
748 Etchegorry, F. S. Olesen, J. L. Privette, Directional viewing effects on
749 satellite land surface temperature products over sparse vegetation canopies-
750 a multisensor analysis, *IEEE Geoscience and Remote Sensing Letters* 10
751 (2013) 1464–1468. URL: <http://dx.doi.org/10.1109/LGRS.2013.2260319>.
752 doi:10.1109/lgrs.2013.2260319.

753 H. Ren, R. Liu, G. Yan, X. Mu, Z.-L. Li, F. Nerry, Q. Liu, Angular normaliza-
754 tion of land surface temperature and emissivity using multiangular middle and
755 thermal infrared data, *IEEE Transactions on Geoscience and Remote Sensing* 52
756 (2014) 4913–4931. URL: <http://dx.doi.org/10.1109/tgrs.2013.2285924>.
757 doi:10.1109/tgrs.2013.2285924.

758 J. B. Fisher, B. Lee, A. J. Purdy, G. H. Halverson, M. B. Dohlen, K. Cawse-Nicholson,
759 A. Wang, R. G. Anderson, B. Aragon, M. A. Arain, et al., Ecostress: Nasa’s next
760 generation mission to measure evapotranspiration from the international space sta-
761 tion, *Water Resources Research* 56 (2020) e2019WR026058.

762 G. Hulley, S. Hook, Ecostress level-2 lst and emissivity algorithm theoretical basis
763 document (atbd)(no. jpl d-94643), Jet Propulsion Laboratory, California Institute of
764 Technology (2018).

765 D. Roy, M. Wulder, T. Loveland, W. C.E., R. Allen, M. Anderson, D. Helder, J. Irons,
766 D. Johnson, R. Kennedy, T. Scambos, C. Schaaf, J. Schott, Y. Sheng, E. Vermote,
767 A. Belward, R. Bindschadler, W. Cohen, F. Gao, J. Hipple, P. Hostert, J. Huntington,
768 C. Justice, A. Kilic, V. Kovalskyy, Z. Lee, L. Lyburner, J. Masek, J. McCorkel,

- 769 Y. Shuai, R. Trezza, J. Vogelmann, R. Wynne, Z. Zhu, Landsat-8: Science and
770 product vision for terrestrial global change research, *Remote Sensing of Environ-*
771 *ment* 145 (2014) 154–172. URL: [http://dx.doi.org/10.1016/j.rse.2014.](http://dx.doi.org/10.1016/j.rse.2014.02.001)
772 [02.001](http://dx.doi.org/10.1016/j.rse.2014.02.001). doi:10.1016/j.rse.2014.02.001.
- 773 S. J. Hook, J. J. Myers, K. J. Thome, M. Fitzgerald, A. B. Kahle, The modis/aster
774 airborne simulator (master)—a new instrument for earth science studies, *Remote*
775 *Sensing of Environment* 76 (2001) 93–102.
- 776 G. C. Hulley, S. J. Hook, E. Abbott, N. Malakar, T. Islam, M. Abrams, The aster global
777 emissivity dataset (aster ged): Mapping earth’s emissivity at 100 meter spatial scale,
778 *Geophysical Research Letters* 42 (2015) 7966–7976. URL: [http://dx.doi.org/](http://dx.doi.org/10.1002/2015GL065564)
779 [10.1002/2015GL065564](http://dx.doi.org/10.1002/2015GL065564). doi:10.1002/2015gl065564.
- 780 A. Berk, P. Conforti, R. Kennett, T. Perkins, F. Hawes, J. van den Bosch, Modtran6: a
781 major upgrade of the modtran radiative transfer code, in: *Algorithms and Technolo-*
782 *gies for Multispectral, Hyperspectral, and Ultraspectral Imagery XX*, 2014, p. nil.
783 URL: <http://dx.doi.org/10.1117/12.2050433>. doi:10.1117/12.2050433.
- 784 R. Gelaro, W. McCarty, M. J. Suárez, R. Todling, A. Molod, L. Takacs, C. A. Ran-
785 dles, A. Darmenov, M. G. Bosilovich, R. Reichle, K. Wargan, L. Coy, R. Cul-
786 lather, C. Draper, S. Akella, V. Buchard, A. Conaty, A. M. da Silva, W. Gu, G.-
787 K. Kim, R. Koster, R. Lucchesi, D. Merkova, J. E. Nielsen, G. Partyka, S. Paw-
788 son, W. Putman, M. Rienecker, S. D. Schubert, M. Sienkiewicz, B. Zhao, The
789 modern-era retrospective analysis for research and applications, version 2 (merra-2),
790 *Journal of Climate* 30 (2017) 5419–5454. URL: [http://dx.doi.org/10.1175/](http://dx.doi.org/10.1175/JCLI-D-16-0758.1)
791 [JCLI-D-16-0758.1](http://dx.doi.org/10.1175/JCLI-D-16-0758.1). doi:10.1175/jcli-d-16-0758.1.
- 792 N. K. Malakar, G. C. Hulley, S. J. Hook, K. Laraby, M. Cook, J. R. Schott, An
793 operational land surface temperature product for landsat thermal data: Methodol-
794 ogy and validation, *IEEE Transactions on Geoscience and Remote Sensing* 56
795 (2018) 5717–5735. URL: <http://dx.doi.org/10.1109/TGRS.2018.2824828>.
796 doi:10.1109/tgrs.2018.2824828.

- 797 S. J. Hook, et al., HypsIRI Level-2 Thermal Infrared (TIR) land surface temperature
798 and emissivity algorithm theoretical basis document., Technical Report, Pasadena,
799 CA: Jet Propulsion Laboratory, National Aeronautics and Space . . . , 2011.
- 800 D. Hoese, P. Lahtinen, M. Raspaud, W. Roberts, Lavergne, S. Bot, G. Holl,
801 S. Finkensieper, G. Ghiggi, A. Dybbroe, X. Zhang, M. Itkin, A. Meraner,
802 BENR0, A. Valentino, Nina, L. Ørum Rasmussen, lorenzo clementi, M. Val-
803 gur, D. Rykov, A. Brammer, B. Hawkins, F. Pinault, storpipfugl, owenlittlejohns,
804 A. R. P. Morena, B. Couwenberg, B. Esse, pytroll/pyresample: Version 1.26.0 post
805 0, 2022. URL: <https://doi.org/10.5281/zenodo.7358887>. doi:10.5281/
806 [zenodo.7358887](https://doi.org/10.5281/zenodo.7358887).
- 807 L. Su, X. Li, M. Friedl, A. Strahler, X. Gu, Kernel-driven model of effective directional
808 emissivity for non-isothermal surfaces, Progress in Natural Science 12 (2002) 603–
809 607.
- 810 J.-P. Lagouarde, M. Irvine, Directional anisotropy in thermal infrared measurements
811 over toulouse city centre during the capitoul measurement campaigns: First results,
812 Meteorology and Atmospheric Physics 102 (2008) 173–185. URL: [http://dx.](http://dx.doi.org/10.1007/s00703-008-0325-4)
813 [doi.org/10.1007/s00703-008-0325-4](http://dx.doi.org/10.1007/s00703-008-0325-4). doi:10.1007/s00703-008-0325-4.
- 814 P. Virtanen, R. Gommers, T. E. Oliphant, M. Haberland, T. Reddy, D. Cournapeau,
815 E. Burovski, P. Peterson, W. Weckesser, J. Bright, S. J. van der Walt, M. Brett,
816 J. Wilson, K. J. Millman, N. Mayorov, A. R. J. Nelson, E. Jones, R. Kern, E. Larson,
817 C. J. Carey, Í. Polat, Y. Feng, E. W. Moore, J. VanderPlas, D. Laxalde, J. Perktold,
818 R. Cimrman, I. Henriksen, E. A. Quintero, C. R. Harris, A. M. Archibald, A. H.
819 Ribeiro, F. Pedregosa, P. van Mulbregt, A. Vijaykumar, A. P. Bardelli, A. Roth-
820 berg, A. Hilboll, A. Kloeckner, A. Scopatz, A. Lee, A. Rokem, C. N. Woods,
821 C. Fulton, C. Masson, C. Häggström, C. Fitzgerald, D. A. Nicholson, D. R. Hagen,
822 D. V. Pasechnik, E. Olivetti, E. Martin, E. Wieser, F. Silva, F. Lenders, F. Wilhelm,
823 G. Young, G. A. Price, G.-L. Ingold, G. E. Allen, G. R. Lee, H. Audren, I. Probst,
824 J. P. Dietrich, J. Silterra, J. T. Webber, J. Slavič, J. Nothman, J. Buchner, J. Kulick,
825 J. L. Schönberger, J. V. de Miranda Cardoso, J. Reimer, J. Harrington, J. L. C. Ro-

826 dríguez, J. Nunez-Iglesias, J. Kuczynski, K. Tritz, M. Thoma, M. Newville, M. Küm-
827 merer, M. Bolingbroke, M. Tartre, M. Pak, N. J. Smith, N. Nowaczyk, N. Shebanov,
828 O. Pavlyk, P. A. Brodtkorb, P. Lee, R. T. McGibbon, R. Feldbauer, S. Lewis, S. Ty-
829 gier, S. Sievert, S. Vigna, S. Peterson, S. More, T. Pudlik, T. Oshima, T. J. Pin-
830 gel, T. P. Robitaille, T. Spura, T. R. Jones, T. Cera, T. Leslie, T. Zito, T. Krauss,
831 U. Upadhyay, Y. O. Halchenko, Y. Vázquez-Baeza, S. . Contributors, Scipy
832 1.0: Fundamental algorithms for scientific computing in python, Nature Methods
833 17 (2020) 261–272. URL: <http://dx.doi.org/10.1038/s41592-019-0686-2>.
834 doi:10.1038/s41592-019-0686-2.

835 N.-E. Tsendbazar, A. Tarko, L. Li, M. Herold, M. Lesiv, S. Fritz, V. Maus, Coper-
836 nicus Global Land Service: Land Cover 100m: version 3 Globe 2015-2019:
837 Validation Report, 2021. URL: <https://doi.org/10.5281/zenodo.4723975>.
838 doi:10.5281/zenodo.4723975.

839 F. Kriegler, W. Malila, R. Nalepka, W. Richardson, Preprocessing transformations and
840 their effects on multispectral recognition, Remote sensing of environment, VI (1969)
841 97.

842 R. Niclòs, J. Puchades, C. Coll, M. J. Barberà, L. Pérez-Planells, J. A. Valiente, J. M.
843 Sánchez, Evaluation of landsat-8 tirs data recalibrations and land surface temper-
844 ature split-window algorithms over a homogeneous crop area with different pheno-
845 logical land covers, ISPRS Journal of Photogrammetry and Remote Sensing 174
846 (2021) 237–253. URL: [http://dx.doi.org/10.1016/j.isprsjprs.2021.02.](http://dx.doi.org/10.1016/j.isprsjprs.2021.02.005)
847 [005](http://dx.doi.org/10.1016/j.isprsjprs.2021.02.005). doi:10.1016/j.isprsjprs.2021.02.005.

848 D. Phiri, M. Simwanda, S. Salekin, V. R. Nyirenda, Y. Murayama, M. Ranagalage,
849 Sentinel-2 data for land cover/use mapping: A review, Remote Sensing 12 (2020)
850 2291.

851 J.-P. Lagouarde, A. Hénon, B. Kurz, P. Moreau, M. Irvine, J. Voogt, P. Mestayer, Mod-
852 elling daytime thermal infrared directional anisotropy over toulouse city centre, Re-
853 mote Sensing of Environment 114 (2010) 87–105. URL: [http://dx.doi.org/10.](http://dx.doi.org/10.1016/j.rse.2009.08.012)
854 [1016/j.rse.2009.08.012](http://dx.doi.org/10.1016/j.rse.2009.08.012). doi:10.1016/j.rse.2009.08.012.

- 855 L. Jiang, W. Zhan, L. Hu, F. Huang, F. Hong, Z. Liu, J. Lai, C. Wang, Assessment
856 of different kernel-driven models for daytime urban thermal radiation directionality
857 simulation, *Remote Sensing of Environment* 263 (2021) 112562. URL: [http://dx.](http://dx.doi.org/10.1016/j.rse.2021.112562)
858 [doi.org/10.1016/j.rse.2021.112562](http://dx.doi.org/10.1016/j.rse.2021.112562). doi:10.1016/j.rse.2021.112562.
- 859 J. Michel, O. Hagolle, S. J. Hook, J.-L. Roujean, P. Gamet, Master and Landsat-8
860 simultaneous acquisition datacubes for the quantification of directional anisotropy
861 in Thermal Infra-Red domain, 2023. URL: [https://doi.org/10.5281/zenodo.](https://doi.org/10.5281/zenodo.7757028)
862 [7757028](https://doi.org/10.5281/zenodo.7757028). doi:10.5281/zenodo.7757028.